

Cosmological constraints from higher-redshift gamma-ray burst, H II starburst galaxy, and quasar (and other) data

Shulei Cao,^{1*} Joseph Ryan,^{1†} Narayan Khadka,^{1‡} Bharat Ratra^{1§}

¹*Department of Physics, Kansas State University, 116 Cardwell Hall, Manhattan, KS 66502, USA*

Accepted XXX. Received YYY; in original form ZZZ

ABSTRACT

We use higher-redshift gamma-ray burst (GRB), H II starburst galaxy (H II G), and quasar angular size (QSO-AS) measurements to constrain six spatially flat and non-flat cosmological models. These three sets of cosmological constraints are mutually consistent. Cosmological constraints from a joint analysis of these data sets are largely consistent with currently-accelerating cosmological expansion as well as with cosmological constraints derived from a combined analysis of Hubble parameter ($H(z)$) and baryon acoustic oscillation (BAO, with Planck-determined baryonic matter density) measurements. A joint analysis of the $H(z) + \text{BAO} + \text{QSO-AS} + \text{H II G} + \text{GRB}$ data provides fairly model-independent determinations of the non-relativistic matter density parameter $\Omega_{\text{m}_0} = 0.313 \pm 0.013$ and the Hubble constant $H_0 = 69.3 \pm 1.2 \text{ km s}^{-1} \text{ Mpc}^{-1}$. These data are consistent with the dark energy being a cosmological constant and with spatial hypersurfaces being flat, but they do not rule out mild dark energy dynamics or a little spatial curvature. We also investigate the effect of including quasar flux measurements in the mix and find no novel conclusions.

Key words: cosmological parameters – dark energy – cosmology: observations

1 INTRODUCTION

There is a large body of evidence indicating that the Universe recently transitioned from a decelerated to an accelerated phase of expansion (at redshift $z \sim 3/4$; see e.g. Farooq et al. 2017) and has been undergoing accelerated expansion ever since (for reviews, see e.g. Ratra & Vogeley 2008; Martin 2012; Coley & Ellis 2020). In the standard model of cosmology, called the Λ CDM model (Peebles 1984), the accelerated expansion is powered by a constant dark energy density (the cosmological constant, Λ). This model also assumes that spatial hypersurfaces are flat on cosmological scales, and that the majority of non-relativistic matter in the Universe consists of cold dark matter (CDM).

Out of all the models that have been devised to explain the observed accelerated expansion of the Universe, the Λ CDM model is currently the most highly favored in terms of both observational data and theoretical parsimony (see e.g. Farooq et al. 2017; Scolnic et al. 2018; Planck Collaboration 2020; eBOSS Collaboration 2020). In spite of these virtues, however, there are some indications that the Λ CDM model may not tell the whole story. On the observational side, some workers have found evidence of discrepancies

between the Λ CDM model and cosmological observations (Riess 2019; Martinelli & Tutusaus 2019) and on the theoretical side, the origin of Λ has yet to be explained in fundamental terms (e.g., Martin 2012). One way to pin down the nature of dark energy is by studying its dynamics phenomenologically. It is possible that the dark energy density may evolve in time (Peebles & Ratra 1988), and many dark energy models exhibiting this behavior have been proposed.

Cosmological models have largely been tested in the redshift range $0 \lesssim z \lesssim 2.3$, with baryon acoustic oscillation (BAO¹) measurements probing the upper end of this range, and at $z \sim 1100$, using cosmic microwave background (CMB) anisotropy data. To determine the accuracy of our cosmological models, we also need to test them in the redshift range $2.3 \lesssim z \lesssim 1100$. Quasar angular size (QSO-AS), H II starburst galaxy (H II G), quasar X-ray and UV flux (QSO-Flux), and gamma-ray burst (GRB) measurements are some of the handful of data available in this range. The main goal of this paper is, therefore, to examine the effect that QSO-AS, H II G, and GRB data have on cosmologi-

* E-mail: shulei@phys.ksu.edu

† E-mail: jryan@phys.ksu.edu

‡ E-mail: nkhadka@phys.ksu.edu

§ E-mail: ratra@phys.ksu.edu

¹ In our BAO data analyses in this paper the sound horizon computation assumes a value for the current baryonic matter physical density parameter $\Omega_{\text{b}_0} h^2$, appropriate for the model under study, computed from Planck CMB anisotropy data.

cal model parameter constraints, in combination with each other, and in combination with more well-known probes.²

Gamma-ray bursts are promising cosmological probes for two reasons. First, it is believed that they can be used as standardizable candles (Lamb & Reichart 2000, 2001; Amati et al. 2002, 2008, 2009; Ghirlanda et al. 2004; Demianski & Piedipalumbo 2011; Wang et al. 2015). Second, they cover a redshift range that is wider than most other commonly-used cosmological probes, having been observed up to $z \sim 8.2$ (Amati et al. 2008, 2009, 2019; Samushia & Ratra 2010; Demianski & Piedipalumbo 2011; Wang et al. 2016; Demianski et al. 2017, 2019; Fana Dirirsa et al. 2019; Khadka & Ratra 2020c). In particular, the $z \sim 2.7\text{--}8.2$ part of the Universe is primarily accessed by GRBs,³ so if GRBs can be standardized, they could provide useful information about a large, mostly unexplored, part of the Universe.

QSO-AS data currently reach to $z \sim 2.7$. These data, consisting of measurements of the angular size of astrophysical radio sources, furnish a standard ruler that is independent of that provided by the BAO sound horizon scale. The intrinsic linear size l_m of intermediate luminosity QSOs has recently been accurately determined by Cao et al. (2017), opening the way for QSOs to, like GRBs, test cosmological models in a little-explored region of redshift space.⁴

H II G data reach to $z \sim 2.4$, just beyond the range of current BAO data. Measurements of the luminosities of the Balmer lines in H II galaxies can be correlated with the velocity dispersion of the radiating gas, making H II galaxies a standard candle that can complement both GRBs and lower-redshift standard candles like supernovae (Siegel et al. 2005; Plionis et al. 2009; Mania & Ratra 2012; Chávez et al. 2014; González-Morán et al. 2019).

Current QSO-Flux measurements reach to $z \sim 5.1$, but they favor a higher value of the current (denoted by the subscript “0”) non-relativistic matter density parameter (Ω_{m_0}) than what is currently thought to be reasonable. The Ω_{m_0} values obtained using QSO-Flux data, in a number of cosmological models, are in nearly 2σ tension with the values obtained by using other well-established cosmological probes like CMB, BAO, and Type Ia supernovae (Risaliti & Lusso 2019; Yang et al. 2019; Wei & Melia 2020; Khadka & Ratra 2020b). Techniques for standardizing QSO-Flux measurements are still under development, so it might be too early to draw strong conclusions about the cosmological constraints obtained from QSO-Flux measurements. Therefore, in this paper, we use QSO-Flux data alone and in combination with other data to constrain cosmological parameters in four different models, and record these results in Appendix A.

We find that the GRB, H II G, and QSO-AS constraints are largely mutually consistent, and that their joint constraints are consistent with those from more widely used, and more restrictive, BAO and Hubble parameter ($H(z)$)

² We relegate the analysis of QSO-Flux data to an appendix, the reasons for which are discussed there.

³ Though QSO-Flux measurements can reach up to $z \sim 5.1$.

⁴ The use of QSO-AS measurements to constrain cosmological models dates back to near the turn of the century (e.g. Gurvits et al. 1999; Vishwakarma 2001; Lima & Alcaniz 2002; Zhu & Fujimoto 2002; Chen & Ratra 2003), but, as discussed in Ryan et al. (2019), these earlier results are suspect, because they are based on an inaccurate determination of l_m .

data. When used jointly with the $H(z) + \text{BAO}$ data, these higher- z data tighten the $H(z) + \text{BAO}$ constraints.

This paper is organized as follows. In Section 2 we introduce the data we use. Section 3 describes the models we analyze, with a description of our analysis method in Section 4. Our results are in Section 5, and we provide our conclusions in Section 6. Additionally, we discuss our results for QSO-Flux measurements in Appendix A.

2 DATA

We use QSO-AS, H II G, QSO-Flux, and GRB data to obtain constraints on the cosmological models we study. The QSO-AS data, comprising 120 measurements compiled by Cao et al. (2017) (listed in Table 1 of that paper) and spanning the redshift range $0.462 \leq z \leq 2.73$, are also used in Ryan et al. (2019); see these papers for descriptions. The H II G data, comprising 107 low redshift ($0.0088 \leq z \leq 0.16417$) H II G measurements, used in Chávez et al. (2014) (recalibrated by González-Morán et al. 2019), and 46 high redshift ($0.636427 \leq z \leq 2.42935$) H II G measurements, used in González-Morán et al. (2019), are also used in Cao et al. (2020). The GRB data, spanning the redshift range $0.48 \leq z \leq 8.2$, are collected from Fana Dirirsa et al. (2019) (25 from Table 2 of that paper (F10), and the remaining 94 from Table 5 of the same, which are a subset of those compiled by Wang et al. 2016) and also used in Khadka & Ratra (2020c). We also add 1598 QSO-Flux measurements spanning the redshift range $0.036 \leq z \leq 5.1003$, from Risaliti & Lusso (2019). These data are used in Khadka & Ratra (2020b); see that paper for details. Results related to these QSO-Flux data are discussed in Appendix A.

In order to be useful as cosmological probes, GRBs need to be standardized, and many phenomenological relations have been proposed for this purpose (Amati et al. 2002, Ghirlanda et al. 2004, Liang & Zhang 2005, Muccino 2020, and references therein). As in Khadka & Ratra (2020c), we use the Amati relation (Amati et al. 2002), which is an observed correlation between the peak photon energy E_p and the isotropic-equivalent radiated energy E_{iso} of long-duration GRBs, to standardize GRB measurements. There have been many attempts to standardize GRBs using the Amati relation. Some analyses assume a fixed value of Ω_{m_0} to calibrate the Amati relation, so they favor a relatively reasonable value of Ω_{m_0} . Others use supernovae data to calibrate the Amati relation, while some use $H(z)$ data to calibrate it. This means that most previous GRB analyses are affected by some non-GRB external factors. In some cases this leads to a circularity problem, in which the models to be constrained by using the Amati relation are also used to calibrate the Amati relation itself (Liu & Wei 2015; Demianski et al. 2017, 2019; Fana Dirirsa et al. 2019). In other cases, the data used in the calibration process dominate the analysis results. To overcome these problems, we fit the parameters of the Amati relation simultaneously with the parameters of the cosmological models we study (as done in Khadka & Ratra 2020c; also see Wang et al. 2016).

The isotropic radiated energy E_{iso} of a source in its rest frame at a luminosity distance D_L is

$$E_{\text{iso}} = \frac{4\pi D_L^2}{1+z} S_{\text{bolo}}, \quad (1)$$

where S_{bolo} is the bolometric fluence, and D_L (defined below) depends on z and on the parameters of our cosmological models. E_{iso} is connected to the source's peak energy output E_p via the Amati relation (Amati et al. 2008, 2009)

$$\log E_{\text{iso}} = a + b \log E_p, \quad (2)$$

where a and b are free parameters that we vary in our model fits.⁵ Note here that the peak energy $E_p = (1+z)E_{p,\text{obs}}$ where $E_{p,\text{obs}}$ is the observed peak energy.

The correlation between H II G luminosity (L) and velocity dispersion (σ) is:

$$\log L = \beta \log \sigma + \gamma, \quad (3)$$

where β is the slope and γ is the intercept. As in Cao et al. (2020) (see that paper for details), we use the values

$$\beta = 5.022 \pm 0.058, \quad (4)$$

and

$$\gamma = 33.268 \pm 0.083. \quad (5)$$

One can test a cosmological model with parameters \mathbf{p} by using it to compute a theoretical distance modulus

$$\mu_{\text{th}}(\mathbf{p}, z) = 5 \log D_L(\mathbf{p}, z) + 25, \quad (6)$$

and comparing this prediction to the distance modulus computed from observational H II G luminosity and flux (f) data

$$\mu_{\text{obs}} = 2.5 \log L - 2.5 \log f - 100.2, \quad (7)$$

(Terlevich et al. 2015; González-Morán et al. 2019).

QSO-AS data can be used to test cosmological models by comparing the theoretical angular size of the QSO

$$\theta_{\text{th}} = \frac{l_m}{D_A} \quad (8)$$

with its observed angular size θ_{obs} . In equation (8), l_m is the characteristic linear size of the QSO,⁶ and D_A (defined below) is its angular size distance.

Underestimated systematic uncertainties for both H II G and QSO-AS data might be responsible for the large reduced χ^2 (described in Sec. 5.4).

The transverse comoving distance $D_M(\mathbf{p}, z)$ is related to the luminosity distance $D_L(\mathbf{p}, z)$ and the angular size distance $D_A(\mathbf{p}, z)$ through $D_M(\mathbf{p}, z) = D_L(\mathbf{p}, z)/(1+z) = (1+z)D_A(\mathbf{p}, z)$, and is a function of z and the parameters \mathbf{p} :

$$D_M(\mathbf{p}, z) = \begin{cases} D_C(\mathbf{p}, z) & \text{if } \Omega_{k0} = 0, \\ \frac{c}{H_0 \sqrt{\Omega_{k0}}} \sinh [\sqrt{\Omega_{k0}} H_0 D_C(\mathbf{p}, z)/c] & \text{if } \Omega_{k0} > 0, \\ \frac{c}{H_0 \sqrt{|\Omega_{k0}|}} \sin [\sqrt{|\Omega_{k0}|} H_0 D_C(\mathbf{p}, z)/c] & \text{if } \Omega_{k0} < 0. \end{cases} \quad (9)$$

In the preceding equation,

$$D_C(\mathbf{p}, z) \equiv c \int_0^z \frac{dz'}{H(\mathbf{p}, z')}, \quad (10)$$

H_0 is the Hubble constant, Ω_{k0} is the current value of the

⁵ $\log = \log_{10}$ is implied hereinafter.

⁶ For the data sample we use, this quantity is equal to 11.03 ± 0.25 pc; see Cao et al. (2017).

spatial curvature energy density parameter, and c is the speed of light (Hogg 1999).

We also use $H(z)$ and BAO measurements to constrain cosmological parameters. The $H(z)$ data, 31 measurements spanning the redshift range $0.070 \leq z \leq 1.965$, are compiled in Table 2 of Ryan et al. (2018). The BAO data, 11 measurements spanning the redshift range $0.38 \leq z \leq 2.34$, are listed in Table 1 of Cao et al. (2020).

Systematic errors that affect $H(z)$ measurements include assumptions about the stellar metallicity of the galaxies in which cosmic chronometers are found, progenitor bias, the presence of a population of young stars in these galaxies, and assumptions about stellar population synthesis models. These effects were studied in Moresco et al. (2012, 2016, 2018, 2020). Moresco et al. (2020) found that the dominant contribution to the systematic error budget comes from the choice of stellar population synthesis model, which introduces an average systematic error of $\sim 8.9\%$ (though the authors say that this can be reduced to $\sim 4.5\%$ by removing an outlier model from the analysis). The impacts of a population of young stars and of the progenitor bias were found to be negligible in Moresco et al. (2018, 2012), and Moresco et al. (2020) found that the impact of a $\sim 5\text{--}10\%$ uncertainty in the metallicity estimates produces a $\sim 4\text{--}9\%$ systematic error in the $H(z)$ measurements.

The systematic uncertainties of BAO from Alam et al. (2017) (described in Sec. 7) are included in their covariance matrix. The BAO data from Carter et al. (2018) is the combined result of the 6dF Galaxy Survey1 (6dFGS) and the SDSS DR7 MGS, where the systematic effects are described in detail in Jones et al. (2009) and Ross et al. (2015) (negligible), respectively. As described in DES Collaboration (2019b), the BAO systematic uncertainty is 15% of their statistical uncertainty and thus negligible. The same negligible systematic effect applies to the BAO measurement from Ata et al. (2018). de Sainte Agathe et al. (2019) added polynomial terms to the correlation function, so as to test the sensitivity of the slowly-varying part of the correlation function to systematic effects. They found that this shifted the BAO peak position by less than 1σ relative to its position in their fiducial model.

3 COSMOLOGICAL MODELS

In this paper we consider three pairs of flat and non-flat cosmological models, with non-dynamical and dynamical dark energy density.⁷ Since the data we use are at low redshift, we neglect the contribution that radiation makes to the cosmological energy budget.

⁷ Observational constraints on non-flat models are discussed in Farooq et al. (2015), Chen et al. (2016), Yu & Wang (2016), Rana et al. (2017), Ooba et al. (2018a,b,c), Yu et al. (2018), Park & Ratra (2018, 2019a,b,c, 2020), Wei (2018), DES Collaboration (2019a), Coley (2019), Jesus et al. (2020), Handley (2019), Zhai et al. (2020), Li et al. (2020), Geng et al. (2020), Kumar et al. (2020), Efstathiou & Gratton (2020), Di Valentino et al. (2020), Gao et al. (2020), Yang & Gong (2020), Agudelo Ruiz et al. (2020), Velásquez-Toribio & Fabris (2020), and references therein.

In the Λ CDM model the Hubble parameter is

$$H(z) = H_0 \sqrt{\Omega_{m_0}(1+z)^3 + \Omega_{k_0}(1+z)^2 + \Omega_\Lambda}, \quad (11)$$

where H_0 , Ω_{m_0} , and the cosmological constant dark energy density parameter Ω_Λ are the parameters to be constrained, and Ω_{k_0} obeys $\Omega_{k_0} = 1 - \Omega_{m_0} - \Omega_\Lambda$. When $\Omega_{k_0} = 0$ (flat Λ CDM), we only constrain H_0 and Ω_{m_0} , as the value of Ω_Λ is fixed by $\Omega_\Lambda = 1 - \Omega_{m_0}$.

The XCDM parametrization is an extension of the Λ CDM model in which the dark energy equation of state parameter, $w_X = p_X/\rho_X$, is allowed to take values different from -1 , where p_X and ρ_X are the pressure and energy density, respectively, of the dark energy, treated in this case as an ideal, spatially homogeneous X-fluid.⁸ In the XCDM parametrization the Hubble parameter takes the form

$$H(z) = H_0 \sqrt{\Omega_{m_0}(1+z)^3 + \Omega_{k_0}(1+z)^2 + \Omega_{X_0}(1+z)^{3(1+w_X)}}, \quad (12)$$

where Ω_{X_0} is the current value of the X-fluid energy density parameter (its constraints are not reported in this paper) subject to $\Omega_{X_0} = 1 - \Omega_{m_0} - \Omega_{k_0}$. When $w_X = -1$ XCDM reduces to Λ CDM. In the general, non-flat case, the model parameters to be constrained are H_0 , Ω_{m_0} , Ω_{k_0} , and w_X . When $\Omega_{k_0} = 0$ (flat XCDM), we only constrain H_0 , Ω_{m_0} , and w_X , as the value of Ω_{X_0} is fixed by $\Omega_{X_0} = 1 - \Omega_{m_0} - \Omega_{k_0}$.

In the ϕ CDM model, a dynamical scalar field ϕ , whose stress-energy tensor acts like that of a time-variable Λ , characterizes the dark energy, and has a potential energy density

$$V(\phi) = \frac{1}{2} \kappa m_p^2 \phi^{-\alpha}. \quad (13)$$

Here m_p is the Planck mass, $\alpha \geq 0$, and

$$\kappa = \frac{8}{3m_p^2} \left(\frac{\alpha+4}{\alpha+2} \right) \left[\frac{2}{3} \alpha(\alpha+2) \right]^{\alpha/2} \quad (14)$$

(Peebles & Ratra 1988; Ratra & Peebles 1988; Pavlov et al. 2013).⁹ For $\alpha = 0$ the ϕ CDM models reduce to the Λ CDM models.

In this paper we make the approximation, valid for our purposes, that the scalar field is spatially homogeneous. When ϕ is approximated in this way, two coupled nonlinear ordinary differential equations control its dynamics. The first is its equation of motion

$$\ddot{\phi} + 3 \left(\frac{\dot{a}}{a} \right) \dot{\phi} - \frac{1}{2} \alpha \kappa m_p^2 \phi^{-\alpha-1} = 0, \quad (15)$$

⁸ Unlike the Λ CDM and ϕ CDM models, the XCDM parametrization is physically incomplete because it cannot sensibly describe the evolution of spatial inhomogeneities. The XCDM parametrization can be made sensible by allowing for an additional free parameter $c_{s,X}^2 = dp_X/d\rho_X$ and requiring $c_{s,X}^2 > 0$.

⁹ Observational constraints on the ϕ CDM model are discussed in, e.g., Chen & Ratra (2004), Samushia et al. (2007), Yashar et al. (2009), Samushia et al. (2010), Chen & Ratra (2011b), Campanelli et al. (2012), Farooq & Ratra (2013), Farooq et al. (2013), Avsajanishvili et al. (2015), Solà et al. (2017), Zhai et al. (2017), Sangwan et al. (2018), Solà Peracaula et al. (2018, 2019), Ooba et al. (2019), Singh et al. (2019), Ryan et al. (2019), Khadka & Ratra (2020a), Ureña-López & Roy (2020).

and the second is the Friedmann equation

$$\left(\frac{\dot{a}}{a} \right)^2 = \frac{8\pi}{3m_p^2} (\rho_m + \rho_\phi) - \frac{k}{a^2}, \quad (16)$$

where a is the scale factor and an overdot denotes a time derivative. In equation (16), $-k/a^2$ is the spatial curvature term (with $\Omega_{k_0} = 0, > 0, < 0$ corresponding to $k = 0, -1, +1$, respectively), and ρ_m and ρ_ϕ are the non-relativistic matter and scalar field energy densities, respectively, where

$$\rho_\phi = \frac{m_p^2}{32\pi} \left(\dot{\phi}^2 + \kappa m_p^2 \phi^{-\alpha} \right). \quad (17)$$

It follows that the Hubble parameter in ϕ CDM is

$$H(z) = H_0 \sqrt{\Omega_{m_0}(1+z)^3 + \Omega_{k_0}(1+z)^2 + \Omega_\phi(z, \alpha)}, \quad (18)$$

where the scalar field energy density parameter

$$\Omega_\phi(z, \alpha) = \frac{1}{12H_0^2} \left(\dot{\phi}^2 + \kappa m_p^2 \phi^{-\alpha} \right). \quad (19)$$

In the general, non-flat case, the parameters to be constrained are H_0 , Ω_{m_0} , Ω_{k_0} , and α . In the special case that $\Omega_{k_0} = 0$ (flat ϕ CDM), we only constrain H_0 , Ω_{m_0} , and α .

4 DATA ANALYSIS METHODOLOGY

By using the PYTHON module EMCEE (Foreman-Mackey et al. 2013), we perform a Markov chain Monte Carlo (MCMC) analysis to maximize the likelihood function, \mathcal{L} , and thereby determine the best-fitting values of the free parameters. The flat cosmological parameter priors are the same as those used in Cao et al. (2020) and the flat priors of the parameters of the Amati relation are non-zero over $0 \leq \sigma_{\text{ext}} \leq 10$ (described below), $40 \leq a \leq 60$, and $0 \leq b \leq 5$.

The likelihood functions associated with $H(z)$, BAO, HIIg, and QSO-AS data are described in Cao et al. (2020). For GRB data, the natural log of its likelihood function (D'Agostini 2005) is

$$\ln \mathcal{L}_{\text{GRB}} = -\frac{1}{2} \left[\chi_{\text{GRB}}^2 + \sum_{i=1}^{119} \ln \left(2\pi(\sigma_{\text{ext}}^2 + \sigma_{y_i}^2 + b^2 \sigma_{x_i}^2) \right) \right], \quad (20)$$

where

$$\chi_{\text{GRB}}^2 = \sum_{i=1}^{119} \left[\frac{(y_i - bx_i - a)^2}{(\sigma_{\text{ext}}^2 + \sigma_{y_i}^2 + b^2 \sigma_{x_i}^2)} \right], \quad (21)$$

$x = \log \frac{E_p}{\text{keV}}$, $\sigma_x = \frac{\sigma_{E_p}}{E_p \ln 10}$, $y = \log \frac{E_{\text{iso}}}{\text{erg}}$, and σ_{ext} is the extrinsic scatter parameter, which contains the unknown systematic uncertainty. For the GRB with σ_z uncertainty in z ,

$$\sigma_y^2 = \left(\frac{\sigma_{S_{\text{bolo}}}}{S_{\text{bolo}} \ln 10} \right)^2 + \left(\frac{2(1+z) \frac{\partial D_M}{\partial z} + D_M}{(1+z) D_M \ln 10} \sigma_z \right)^2, \quad (22)$$

and for those without z uncertainties $\sigma_z = 0$ (the non-zero σ_z has a negligible effect on our results).

The Akaike Information Criterion (*AIC*) and the Bayesian Information Criterion (*BIC*) are used to compare

the goodness of fit of models with different numbers of parameters, where

$$AIC = -2 \ln \mathcal{L}_{\max} + 2n, \quad (23)$$

and

$$BIC = -2 \ln \mathcal{L}_{\max} + n \ln N. \quad (24)$$

In these equations, \mathcal{L}_{\max} is the maximum value of the relevant likelihood function, n is the number of free parameters of the model under consideration, and N is the number of data points (e.g., for GRB $N = 119$).

5 RESULTS

5.1 H II G, QSO-AS, and GRB constraints, individually

We present the posterior one-dimensional (1D) probability distributions and two-dimensional (2D) confidence regions of the cosmological and Amati relation parameters for the six flat and non-flat models in Figs. 1–6, in gray (GRB), red (H II G), and green (QSO-AS). The unmarginalized best-fitting parameter values are listed in Table 1, along with the corresponding χ^2 , $-2 \ln \mathcal{L}_{\max}$, AIC , BIC , and degrees of freedom ν (where $\nu \equiv N - n$).¹⁰ The values of $\Delta\chi^2$, ΔAIC , and ΔBIC reported in Table 1 are discussed in Section 5.4, where we define $\Delta\chi^2$, ΔAIC , and ΔBIC , respectively, as the differences between the values of the χ^2 , AIC , and BIC associated with a given model and their corresponding minimum values among all models. The marginalized best-fitting parameter values and uncertainties ($\pm 1\sigma$ error bars or 2σ limits) are given in Table 2.¹¹ From Table 2 we find that the QSO-AS constraints on Ω_{m0} are consistent with other results within a 1σ range but with large error bars, ranging from a low of $0.329^{+0.086}_{-0.171}$ (flat ϕ CDM) to a high of $0.364^{+0.083}_{-0.150}$ (flat Λ CDM).

The QSO-AS constraints on H_0 are between $H_0 = 61.91^{+2.83}_{-4.92} \text{ km s}^{-1} \text{ Mpc}^{-1}$ (non-flat ϕ CDM) and $H_0 = 68.39^{+6.14}_{-8.98} \text{ km s}^{-1} \text{ Mpc}^{-1}$ (flat XCDM), with large error bars and relatively low values for non-flat XCDM and the ϕ CDM models.

The non-flat models mildly favor open geometry, but are also consistent, given the large error bars, with spatially-flat hypersurfaces (except for non-flat ϕ CDM, where the open case is favored at 2.76σ). For non-flat Λ CDM, non-flat XCDM, and non-flat ϕ CDM, we find $\Omega_{k0} = 0.017^{+0.184}_{-0.277}$, $\Omega_{k0} = 0.115^{+0.466}_{-0.293}$, and $\Omega_{k0} = 0.254^{+0.304}_{-0.092}$, respectively.¹²

The fits to the QSO-AS data favor dark energy being a cosmological constant but do not strongly disfavor dark energy dynamics. For flat (non-flat) XCDM, $w_X = -1.161^{+0.430}_{-0.679}$ ($w_X = -1.030^{+0.593}_{-0.548}$), and for flat (non-flat)

¹⁰ Note that the χ^2 values listed in Tables 1 and A1 are computed from the best-fitting parameter values and are not necessarily the minimum (especially when including GRB and QSO-Flux data).

¹¹ We use the PYTHON package GETDIST (Lewis 2019) to plot these figures and compute the central values (posterior means) and uncertainties of the free parameters listed in Table 2.

¹² From Table 2 we see that GRB data are also consistent with flat spatial geometry in the non-flat Λ CDM and XCDM cases, but also favor, at 2.92σ , open spatial geometry in the case of non-flat ϕ CDM.

ϕ CDM, 2σ upper limits of α are $\alpha < 2.841$ ($\alpha < 4.752$). In the former case, both results are within 1σ of $w_X = -1$, and in the latter case, both 1D likelihoods peak at $\alpha = 0$.

Constraints on cosmological model parameters derived solely from H II G data are discussed in Sec. 5.1 of Cao et al. (2020), while those derived from GRB data are described in Sec. 5.1 of Khadka & Ratra (2020a) (though there are slight differences coming from the different treatments of H_0 and the different ranges of flat priors used there and here); both are listed in Table 2 here. In contrast to the H II G and QSO-AS data sets, the GRB data alone cannot constrain H_0 because there is a degeneracy between the intercept parameter (a) of the Amati relation and H_0 ; for consistency with the analyses of the H II G and QSO-AS data, we treat H_0 as a free parameter in the GRB data analysis here.

Cosmological constraints obtained using the H II G, QSO-AS, and GRB data sets are mutually consistent, and are also consistent with those obtained from most other cosmological probes. This is partially a consequence of the larger H II G, QSO-AS, and GRB data error bars, which lead to relatively weaker constraints on cosmological parameters when each of these data sets is used alone (see Table 2). However, because the H II G, QSO-AS, and GRB constraints are mutually consistent, we may jointly analyze these data. Their combined cosmological constraints will therefore be more restrictive than when they are analyzed individually.

We note, from Figs. 1–6, that a significant part of the likelihood of each of these three data sets lies in the parameter space part with currently-accelerating cosmological expansion.

5.2 H II G, QSO-AS, and GRB (HQASG) joint constraints

Because the H II G, QSO-AS, and GRB contours are mutually consistent for all six of the models we study, we jointly analyze these data to obtain HQASG constraints.

The 1D probability distributions and 2D confidence regions of the cosmological and Amati relation parameters from the HQASG data are in Figs. 1–6, in blue, Figs. 7–12, in green, and panels (a) of Figs. A1–A4, in red. The best-fitting results and uncertainties are in Tables 1 and 2.

We find that the HQASG data combination favors currently-accelerating cosmological expansion.

The fit to the HQASG data produces best-fitting values of Ω_{m0} that lie between $0.205^{+0.044}_{-0.094}$ (non-flat ϕ CDM) at the low end, and $0.322^{+0.062}_{-0.044}$ (flat XCDM) at the high end. This range is smaller than the ranges within which Ω_{m0} falls when it is determined from the H II G, QSO-AS, and GRB data individually, but the low and high ends of the range are still somewhat mutually inconsistent, being 2.66σ away from each other. This is a consequence of the low Ω_{m0} value for non-flat ϕ CDM; the Ω_{m0} values for Λ CDM and XCDM are quite consistent with the recent estimate of Planck Collaboration (2020). In contrast, the best-fitting values of H_0 that we measure from the HQASG data are mutually very consistent (within 0.65σ), with $H_0 = 70.30 \pm 1.68 \text{ km s}^{-1} \text{ Mpc}^{-1}$ (flat ϕ CDM) at the low end of the range and $H_0 = 72.00^{+1.99}_{-1.98} \text{ km s}^{-1} \text{ Mpc}^{-1}$ (flat XCDM) at the high end of the range. These measurements are 0.83σ (flat XCDM) and 1.70σ (flat ϕ CDM) lower than the local Hubble constant measurement of $H_0 = 74.03 \pm 1.42 \text{ km s}^{-1} \text{ Mpc}^{-1}$ (Riess

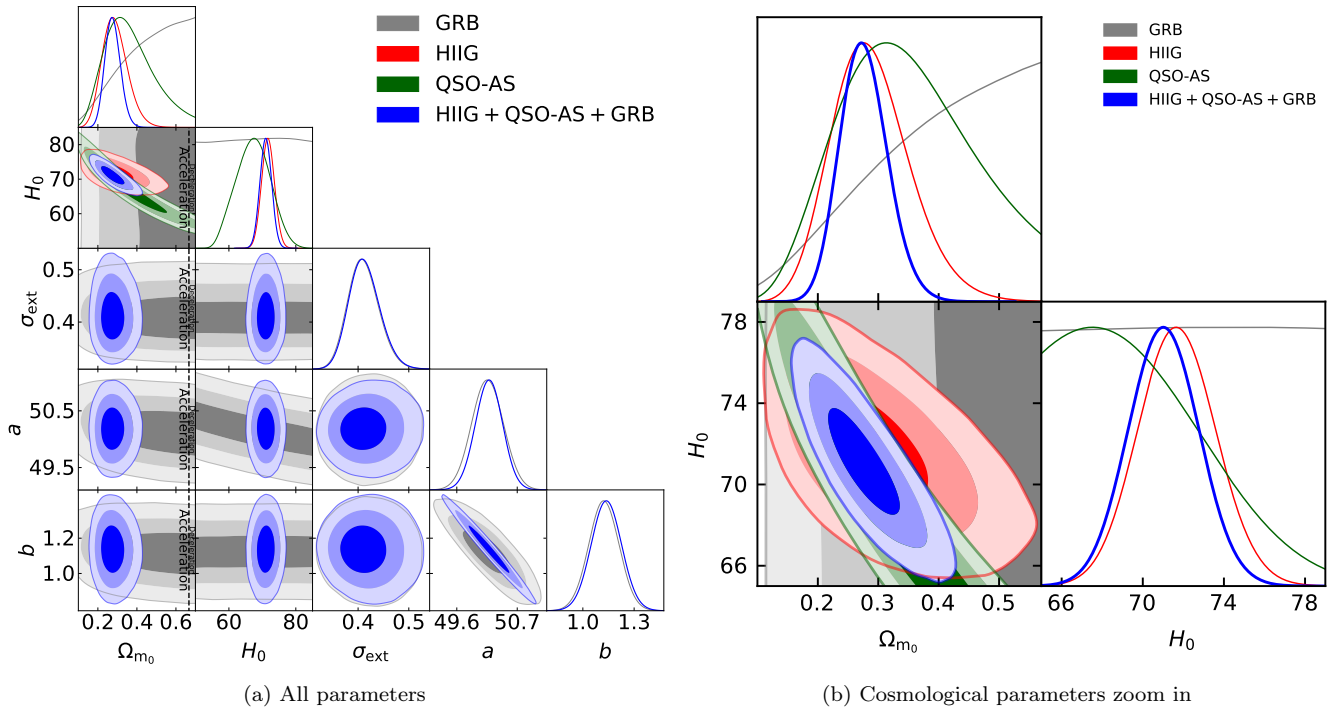


Figure 1. 1σ , 2σ , and 3σ confidence contours for flat Λ CDM, where the right panel is the cosmological parameters comparison zoomed in. The black dotted lines in the left sub-panels of the left panel are the zero-acceleration lines, which divide the parameter space into regions associated with currently-accelerating (left) and currently-decelerating (right) cosmological expansion.

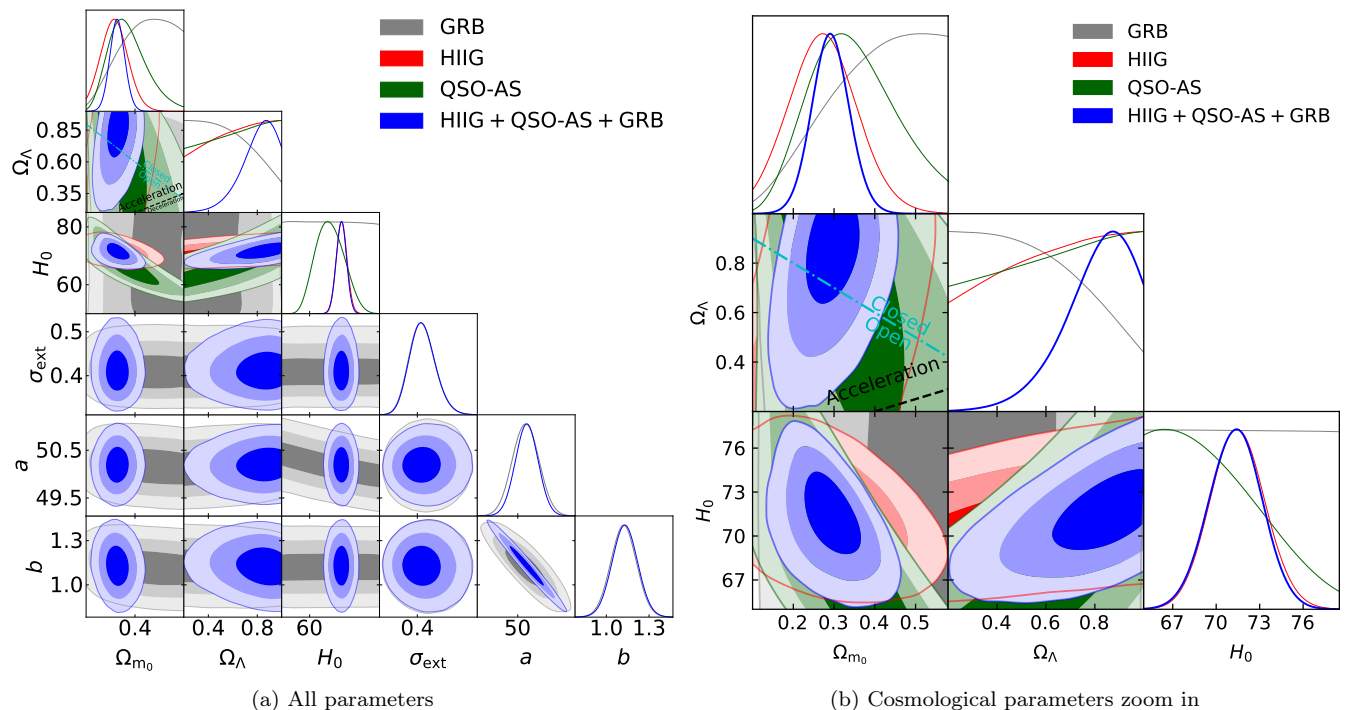


Figure 2. Same as Fig. 1 but for non-flat Λ CDM. The cyan dash-dot line represents the flat Λ CDM case, with closed spatial hypersurfaces to the upper right. The black dotted line is the zero-acceleration line, which divides the parameter space into regions associated with currently-accelerating (above left) and currently-decelerating (below right) cosmological expansion.

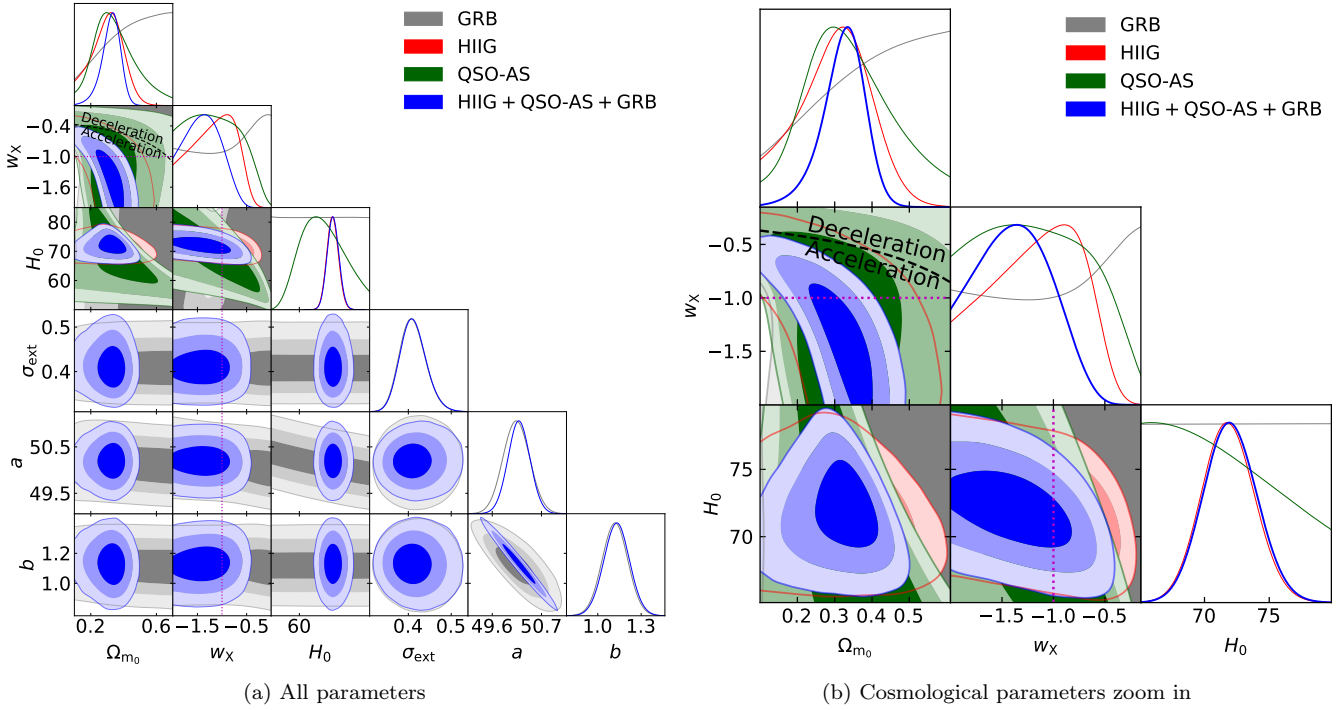


Figure 3. 1σ , 2σ , and 3σ confidence contours for flat XCDM. The black dotted line is the zero-acceleration line, which divides the parameter space into regions associated with currently-accelerating (below left) and currently-decelerating (above right) cosmological expansion. The magenta lines denote $w_X = -1$, i.e. the flat Λ CDM model.

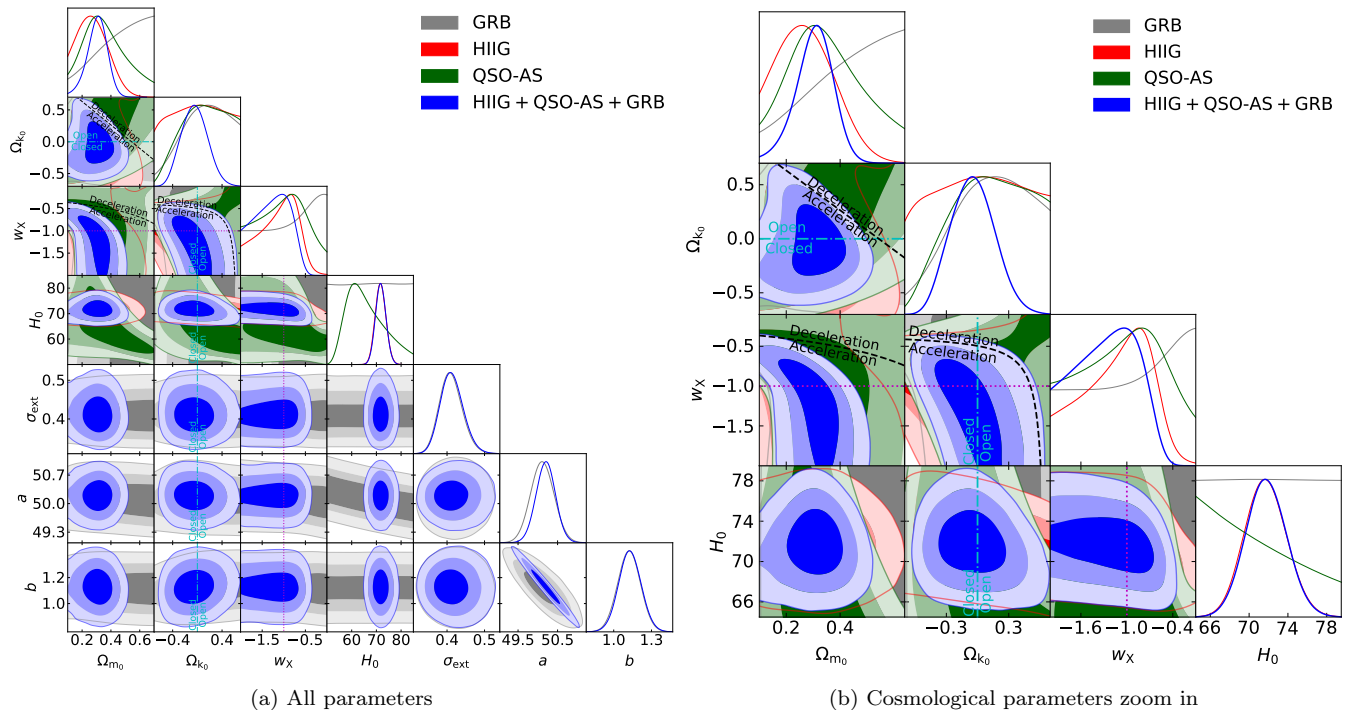


Figure 4. Same as Fig. 3 but for non-flat XCDM, where the zero acceleration lines in each of the three subpanels are computed for the third cosmological parameter set to the $H(z) + \text{BAO}$ data best-fitting values listed in Table 1. Currently-accelerating cosmological expansion occurs below these lines. The cyan dash-dot lines represent the flat XCDM case, with closed spatial hypersurfaces either below or to the left. The magenta lines indicate $w_X = -1$, i.e. the non-flat Λ CDM model.

et al. 2019), and 0.70σ (flat ϕ CDM) and 1.16σ (flat XCDM) higher than the median statistics estimate of $H_0 = 68 \pm 2.8$ km s $^{-1}$ Mpc $^{-1}$ (Chen & Ratra 2011a).¹³

In contrast to the H II G, QSO-AS, and GRB only cases, when fitted to the HQASG data combination the non-flat models mildly favor closed spatial hypersurfaces. For non-flat Λ CDM, non-flat XCDM, and non-flat ϕ CDM, we find $\Omega_{k0} = -0.093^{+0.092}_{-0.190}$, $\Omega_{k0} = -0.044^{+0.193}_{-0.217}$, and $\Omega_{k0} = -0.124^{+0.127}_{-0.253}$, respectively, with the non-flat Λ CDM model favoring closed spatial hypersurfaces at 1.01σ .

The fit to the HQASG data combination produces stronger evidence for dark energy dynamics in the flat and non-flat XCDM parametrizations but weaker evidence in the flat and non-flat ϕ CDM models (in comparison to the H II G and QSO-AS only cases) with tighter error bars on the measured values of w_X and α . For flat (non-flat) XCDM, $w_X = -1.379^{+0.361}_{-0.375}$ ($w_X = -1.273^{+0.501}_{-0.321}$), with $w_X = -1$ being within the 1σ range for non-flat XCDM and being 1.05σ larger for flat XCDM. For flat (non-flat) ϕ CDM, $\alpha < 2.584$ ($\alpha < 3.414$), where both likelihoods peak at $\alpha = 0$.

The constraints on the Amati relation parameters from the HQASG data are also model-independent, but with slightly larger central values and smaller error bars for the parameter a . A reasonable summary is $\sigma_{\text{ext}} = 0.413^{+0.026}_{-0.032}$, $a = 50.19 \pm 0.24$, and $b = 1.133 \pm 0.086$.

The HQASG cosmological constraints are largely consistent with those from other data, like the constraints from the $H(z) + \text{BAO}$ data used in Cao et al. (2020) and Khadka & Ratra (2020c), that are shown in red in Figs. 7–12. We note, however, that there is some mild tension between ϕ CDM Ω_{m0} values, and between XCDM and ϕ CDM H_0 values determined from $H(z) + \text{BAO}$ and HQASG data, with the 2.46σ difference between Ω_{m0} values estimated from the two different data combinations in the non-flat ϕ CDM model being the only somewhat troubling difference (see Table 2).

5.3 $H(z)$, BAO, H II G, QSO-AS, and GRB (HzHQASG) constraints

Given the good mutual consistency between constraints derived from $H(z) + \text{BAO}$ data and those derived from HQASG data, in this subsection we determine more restrictive joint constraints from the combined $H(z)$, BAO, H II G, QSO-AS, and GRB (HzHQASG) data on the parameters of our six cosmological models.

The 1D probability distributions and 2D confidence regions of the cosmological and Amati relation parameters for

¹³ Other local expansion rate determinations have slightly lower central values with slightly larger error bars (Rigault et al. 2015; Zhang et al. 2017; Dhawan et al. 2018; Fernández Arenas et al. 2018; Freedman et al. 2019, 2020; Rameez & Sarkar 2019; Breuval et al. 2020; Efstathiou 2020; Khetan et al. 2020). Our H_0 measurements are consistent with earlier median statistics estimates (Gott et al. 2001; Chen et al. 2003) and with other recent H_0 determinations (Chen et al. 2017; DES Collaboration 2018; Gómez-Valent & Amendola 2018; Planck Collaboration 2020; Zhang 2018; Domínguez et al. 2019; Martinelli & Tutzus 2019; Cuceu et al. 2019; Zeng & Yan 2019; Schöneberg et al. 2019; Lin & Ishak 2019; Blum et al. 2020; Lyu et al. 2020; Philcox et al. 2020; Zhang & Huang 2020; Birrer et al. 2020; Denzel et al. 2020).

all models from the HzHQASG data are in blue in Figs. 7–12, and in red in panels (b) of Figs. A1–A4. The best-fitting results and uncertainties are in Tables 1 and 2.

The measured values of Ω_{m0} here are a little larger, and significantly more restrictively constrained, than the ones in the HQASG cases (except for flat XCDM), being between 0.310 ± 0.014 (non-flat XCDM) and 0.320 ± 0.013 (flat ϕ CDM). The H_0 measurements are a little lower, and more tightly constrained, than in the HQASG cases, and are in better agreement with the lower median statistics estimate of H_0 (Chen & Ratra 2011a) than the higher local expansion rate measurement of H_0 (Riess et al. 2019), being between $68.16^{+1.01}_{-0.80}$ km s $^{-1}$ Mpc $^{-1}$ (flat ϕ CDM) and $69.85^{+1.42}_{-1.55}$ km s $^{-1}$ Mpc $^{-1}$ (flat XCDM).

For non-flat Λ CDM, non-flat XCDM, and non-flat ϕ CDM, we measure $\Omega_{k0} = -0.019^{+0.043}_{-0.048}$, $\Omega_{k0} = -0.024^{+0.092}_{-0.093}$, and $\Omega_{k0} = -0.094^{+0.082}_{-0.064}$, respectively, where the central values are a little higher (closer to 0) than what was measured in the HQASG cases. The joint constraints are more restrictive, with non-flat Λ CDM and XCDM within 0.44σ and 0.26σ of $\Omega_{k0} = 0$, respectively. The non-flat ϕ CDM model, on the other hand, still favors a closed geometry with an Ω_{k0} that is 1.15σ away from zero.

The HzHQASG case has slightly larger measured values and tighter error bars for w_X and α than the HQASG case, so there is also not much evidence in support of dark energy dynamics. For flat (non-flat) XCDM, $w_X = -1.050^{+0.090}_{-0.081}$ ($w_X = -1.019^{+0.202}_{-0.099}$). For flat (non-flat) ϕ CDM, the 2σ upper limits are $\alpha < 0.418$ ($\alpha < 0.905$).

The cosmological model-independent constraints from the HzHQASG data combination on the parameters of the Amati relation can be summarized as $\sigma_{\text{ext}} = 0.412^{+0.026}_{-0.032}$, $a = 50.19 \pm 0.24$, and $b = 1.132 \pm 0.085$.

5.4 Model comparison

From Table 1, we see that the reduced χ^2 values determined from GRB data alone are around unity for all models (being between 1.03 and 1.06) while those values determined from the $H(z) + \text{BAO}$ data combination range from 0.48 to 0.53, with the lower reduced χ^2 here being due to the $H(z)$ data (that probably have overestimated error bars). As discussed in Ryan et al. (2019) and Cao et al. (2020), the cases that involve H II G and QSO-AS data have a larger reduced χ^2 (between 2.11 and 3.02), which is probably due to underestimated systematic uncertainties in both cases.

Based on the *AIC* and the *BIC* (see Table 1), the flat Λ CDM model remains the most favored model, across all data combinations, among the six models we study.¹⁴ From ΔAIC and ΔBIC , we find mostly weak or positive evidence against the models we considered, and only in a few cases do we find strong evidence against them. According to ΔBIC , the evidence against non-flat XCDM is strong for the H II G, QSO-AS, and GRB only cases, and very strong

¹⁴ Note that based on the $\Delta\chi^2$ results of Table 1 non-flat Λ CDM has the minimum χ^2 in the HQASG case and non-flat XCDM has the minimum χ^2 in the H II G, QSO-AS, and $H(z) + \text{BAO}$ cases, whereas non-flat ϕ CDM has the minimum χ^2 for the GRB and HzHQASG cases. The $\Delta\chi^2$ values do not, however, penalize a model for having more parameters.

Table 1. Unmarginalized best-fitting parameter values for all models from various combinations of data.

Model	Data set	Ω_{m0}	Ω_Λ	Ω_{k0}	w_X	α	H_0^c	σ_{ext}	a	b	χ^2	ν	$-2 \ln \mathcal{L}_{\max}$	AIC	BIC	$\Delta\chi^2$	ΔAIC	ΔBIC
Flat Λ CDM	GRB	0.698	0.302	–	–	–	80.36	0.404	49.92	1.113	117.98	114	130.12	140.12	154.01	1.08	0.00	0.00
	H II G	0.276	0.724	–	–	–	71.81	–	–	–	410.75	151	410.75	414.75	420.81	3.15	0.00	0.00
	QSO-AS	0.315	0.685	–	–	–	68.69	–	–	–	352.05	118	352.05	356.05	361.62	1.76	0.00	0.00
	HQASG ^d	0.271	0.729	–	–	–	71.13	0.407	50.18	1.138	879.42	387	895.05	905.05	924.91	0.12	0.00	0.00
	$H(z) + \text{BAO}$	0.314	0.686	–	–	–	68.53	–	–	–	20.82	40	20.82	24.82	28.29	2.39	0.00	0.00
	HzBHQASG ^e	0.317	0.683	–	–	–	69.06	0.404	50.19	1.134	903.61	429	917.79	927.79	948.16	4.05	0.00	0.00
Non-flat Λ CDM	GRB	0.691	0.203	0.106	–	–	77.03	0.402	49.96	1.115	117.37	113	129.96	141.96	158.64	0.47	1.84	4.63
	H II G	0.311	1.000	-0.311	–	–	72.41	–	–	–	410.44	150	410.44	416.44	425.53	2.84	1.69	4.72
	QSO-AS	0.266	1.000	-0.268	–	–	74.73	–	–	–	351.30	117	351.30	357.30	365.66	1.01	1.25	4.04
	HQASG ^d	0.291	0.876	-0.167	–	–	72.00	0.406	50.22	1.120	879.30	386	894.02	906.02	929.85	0.00	0.97	4.94
	$H(z) + \text{BAO}$	0.308	0.643	0.049	–	–	67.52	–	–	–	20.52	39	20.52	26.52	31.73	2.09	1.70	3.44
	HzBHQASG ^e	0.309	0.716	-0.025	–	–	69.77	0.402	50.17	1.141	904.47	428	917.17	929.17	953.61	4.91	1.38	5.45
Flat XCDM	GRB	0.102	–	–	-0.148	–	55.30	0.400	50.22	1.117	118.28	113	129.79	141.79	158.47	1.38	1.67	4.46
	H II G	0.251	–	–	-0.899	–	71.66	–	–	–	410.72	150	410.72	416.72	425.82	3.12	1.97	5.01
	QSO-AS	0.267	–	–	-2.000	–	81.70	–	–	–	351.84	117	351.84	357.84	366.20	1.55	1.79	4.58
	HQASG ^d	0.320	–	–	-1.306	–	72.03	0.404	50.20	1.131	880.47	386	894.27	906.27	930.10	1.17	1.22	5.19
	$H(z) + \text{BAO}$	0.319	–	–	-0.865	–	65.83	–	–	–	19.54	39	19.54	25.54	30.76	1.11	0.72	2.47
	HzBHQASG ^e	0.313	–	–	-1.052	–	69.90	0.407	50.19	1.132	902.09	428	917.55	929.55	953.99	2.53	1.76	5.83
Non-flat XCDM	GRB	0.695	–	0.556	-1.095	–	57.64	0.399	50.13	1.133	118.43	112	129.73	143.73	163.19	1.53	3.61	9.18
	H II G	0.100	–	-0.702	-0.655	–	72.57	–	–	–	407.60	149	407.60	415.60	427.72	0.00	0.85	6.91
	QSO-AS	0.100	–	-0.548	-0.670	–	74.04	–	–	–	350.29	116	350.29	358.29	369.44	0.00	2.24	7.82
	HQASG ^d	0.300	–	-0.161	-1.027	–	80.36	0.405	50.21	1.122	879.48	385	894.01	908.01	935.81	0.18	2.96	10.90
	$H(z) + \text{BAO}$	0.327	–	-0.159	-0.730	–	65.97	–	–	–	18.43	38	18.43	26.43	33.38	0.00	1.61	5.09
	HzBHQASG ^e	0.312	–	-0.045	-0.959	–	69.46	0.402	50.23	1.117	904.17	427	917.07	931.07	959.58	4.61	3.28	11.42
Flat ϕ CDM	GRB	0.674	–	–	–	2.535	84.00	0.399	49.88	1.104	119.15	113	130.14	142.14	158.82	2.25	2.02	4.81
	H II G	0.255	–	–	–	0.260	71.70	–	–	–	410.70	150	410.70	416.70	425.80	3.10	1.95	4.99
	QSO-AS	0.319	–	–	–	0.012	68.47	–	–	–	352.05	117	352.05	358.05	366.41	1.76	2.00	4.79
	HQASG ^d	0.282	–	–	–	0.012	70.81	0.402	50.19	1.135	882.56	386	895.28	907.28	931.11	3.26	2.23	6.20
	$H(z) + \text{BAO}$	0.318	–	–	–	0.364	66.04	–	–	–	19.65	39	19.65	25.65	30.86	1.22	0.83	2.57
	HzBHQASG ^e	0.316	–	–	–	0.013	69.15	0.405	50.24	1.114	903.52	428	918.12	930.12	954.56	3.96	2.33	6.40
Non-flat ϕ CDM	GRB	0.664	–	0.188	–	4.269	59.65	0.403	50.17	1.111	116.90	112	129.93	143.93	163.39	0.00	3.81	9.38
	H II G	0.114	–	-0.437	–	2.680	72.14	–	–	–	409.91	149	409.91	417.91	430.03	2.31	3.16	9.22
	QSO-AS	0.100	–	-0.433	–	2.948	72.37	–	–	–	350.98	116	350.98	358.98	370.13	0.69	2.93	8.51
	HQASG ^d	0.276	–	-0.185	–	0.145	72.11	0.402	50.16	1.142	881.09	385	894.24	908.24	936.03	1.79	3.19	11.12
	$H(z) + \text{BAO}$	0.321	–	-0.137	–	0.887	66.41	–	–	–	18.61	39	18.61	26.61	33.56	0.18	1.79	5.27
	HzBHQASG ^e	0.310	–	-0.052	–	0.193	69.06	0.411	50.21	1.126	899.56	427	917.26	931.26	959.77	0.00	3.47	11.61

^c km s⁻¹ Mpc⁻¹.^d H II G + QSO-AS + GRB.^e $H(z) + \text{BAO} + \text{H II G} + \text{QSO-AS} + \text{GRB}$.

for the HQASG and HzBHQASG cases. Similarly, the evidence against flat ϕ CDM is strong for the HQASG and HzBHQASG cases, and the evidence against non-flat ϕ CDM is strong for the H II G, QSO-AS, and GRB only cases, and very strong for the HQASG and HzBHQASG cases.

Among these six models, a comparison of the ΔBIC values from Table 1 shows that the most disfavored model is non-flat ϕ CDM, and that the second most disfavored model is non-flat XCDM. This is especially true when these models are fitted to the HQASG and HzBHQASG data combinations, in which cases non-flat ϕ CDM and non-flat XCDM are very strongly disfavored. These models aren't as strongly disfavored by the AIC , however; from a comparison of the ΔAIC values in Table 1, we see that the evidence against the most disfavored model (non-flat ϕ CDM) is only positive.

6 CONCLUSION

We find that cosmological constraints determined from higher- z GRB, H II G, and QSO-AS data are mutually consistent. It is both reassuring and noteworthy that these higher- z data jointly favor currently-accelerating cosmological expansion, and that their constraints are consistent with the constraints imposed by more widely used and more restrictive

$H(z)$ and BAO data. Using a data set consisting of 31 $H(z)$, 11 BAO, 120 QSO-AS, 153 H II G, and 119 GRB measurements, we jointly constrain the parameters of the GRB Amati relation and of six cosmological models.

The GRB measurements are of special interest because they reach to $z \sim 8.2$ (far beyond the highest $z \sim 2.3$ reached by BAO data) and into a much less studied area of redshift space. Current GRB data do not provide very restrictive constraints on cosmological model parameters, but in the near future we expect there to be more GRB observations (Shirokov et al. 2020) which should improve the GRB data and provide more restrictive cosmological constraints.

Some of our conclusions do not differ significantly between models and so are model-independent. In particular, for the HzBHQASG data (the full data set excluding QSO-Flux data), we find a fairly restrictive summary value of $\Omega_{m0} = 0.313 \pm 0.013$ that agrees well with many other recent measurements. From these data we also find a fairly restrictive summary value of $H_0 = 69.3 \pm 1.2$ km s⁻¹ Mpc⁻¹ that is in better agreement with the results of Chen & Ratra (2011a) and Planck Collaboration (2020) than with the result of Riess et al. (2019); note that we do not take the H_0 tension issue into account (for a review, see Riess 2019). The HzBHQASG measurements are consistent with flat Λ CDM,

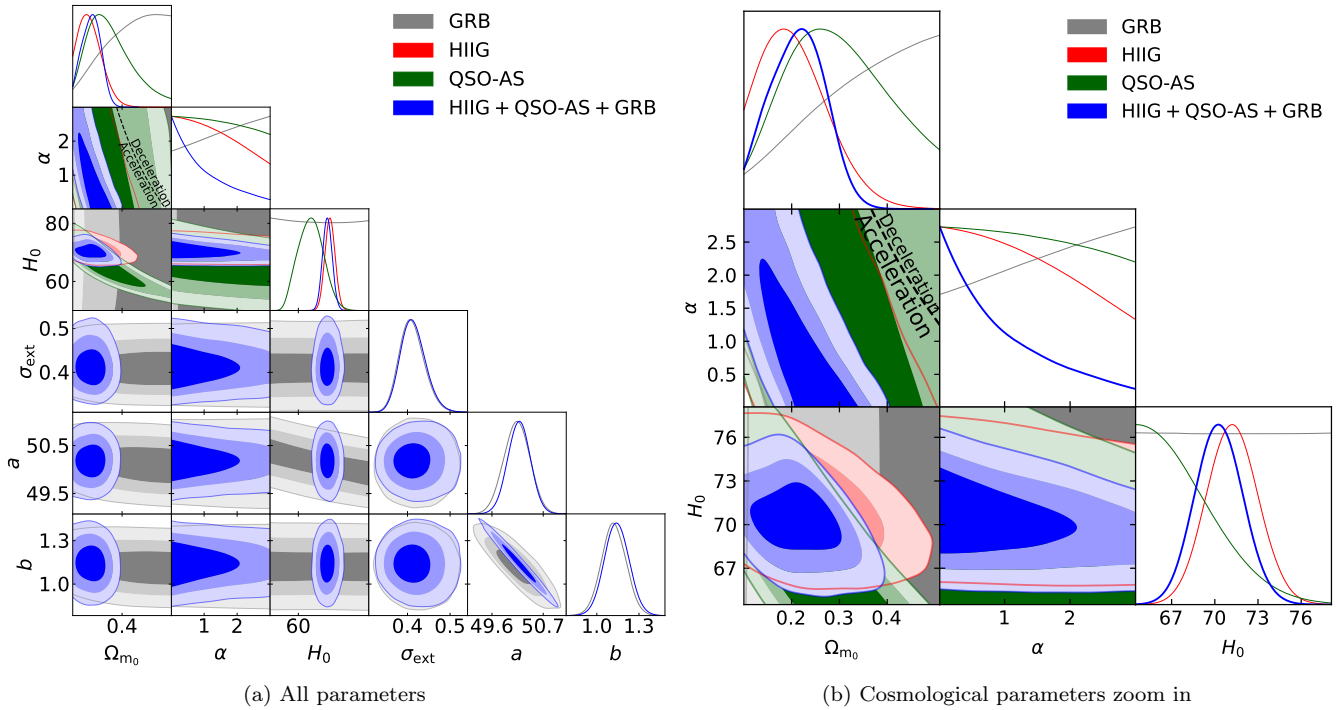


Figure 5. 1σ , 2σ , and 3σ confidence contours for flat ϕ CDM. The black dotted zero-acceleration line splits the parameter space into regions of currently-accelerating (below left) and currently-decelerating (above right) cosmological expansion. The $\alpha = 0$ axis is the flat Λ CDM model.

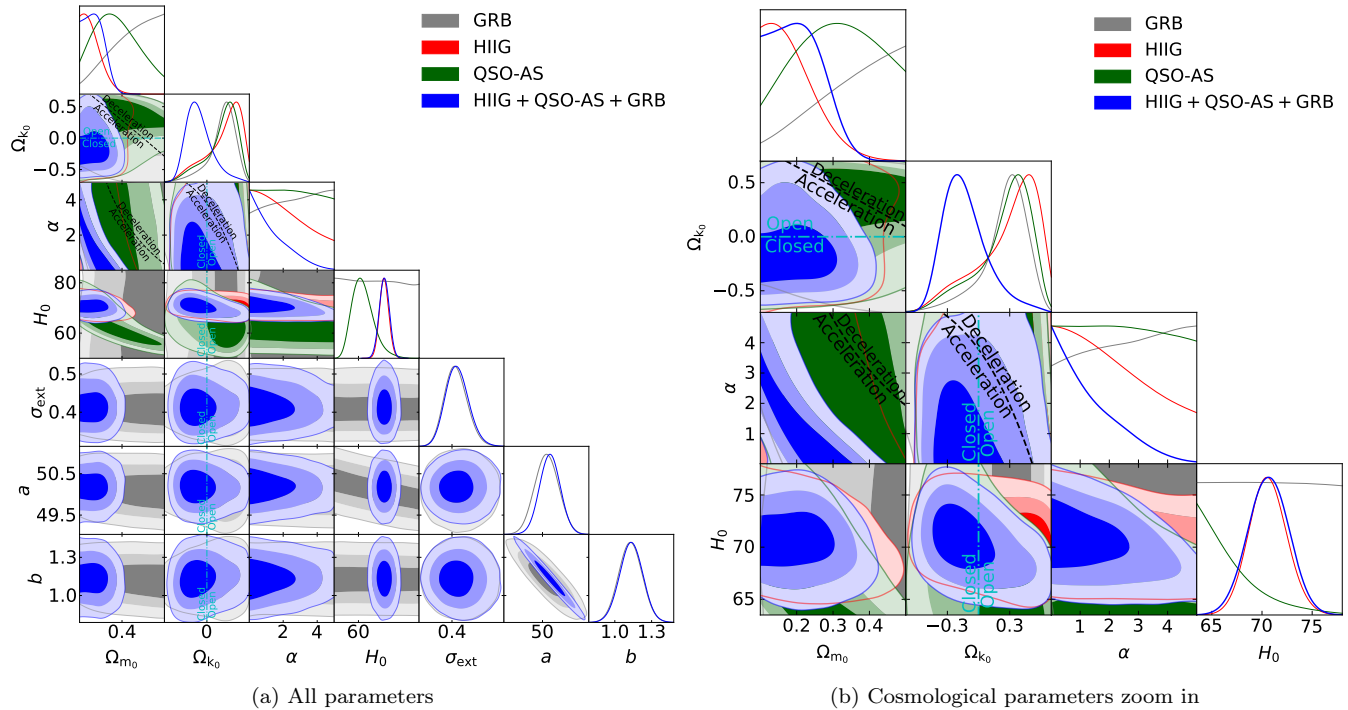


Figure 6. Same as Fig. 5 but for non-flat ϕ CDM, where the zero-acceleration lines in each of the sub-panels are computed for the third cosmological parameter set to the $H(z)$ + BAO data best-fitting values listed in Table 1. Currently-accelerating cosmological expansion occurs below these lines. The cyan dash-dot lines represent the flat ϕ CDM case, with closed spatial geometry either below or to the left. The $\alpha = 0$ axis is the non-flat Λ CDM model.

Table 2. One-dimensional marginalized best-fitting parameter values and uncertainties ($\pm 1\sigma$ error bars or 2σ limits) for all models from various combinations of data.

Model	Data set	Ω_{m0}	Ω_Λ	Ω_{k0}	w_X	α	H_0^c	σ_{ext}	a	b
Flat Λ CDM	GRB	> 0.208	—	—	—	—	—	$0.411^{+0.026}_{-0.032}$	50.16 ± 0.27	1.123 ± 0.085
	H II G	$0.289^{+0.053}_{-0.071}$	—	—	—	—	71.70 ± 1.83	—	—	—
	QSO-AS	$0.364^{+0.083}_{-0.150}$	—	—	—	—	$67.29^{+4.93}_{-5.07}$	—	—	—
	HQASG ^e	$0.277^{+0.034}_{-0.041}$	—	—	—	—	71.03 ± 1.67	$0.413^{+0.026}_{-0.032}$	50.19 ± 0.24	1.138 ± 0.085
	$H(z)$ + BAO	$0.315^{+0.015}_{-0.017}$	—	—	—	—	68.55 ± 0.87	—	—	—
	HzBHQSAG ^f	0.316 ± 0.013	—	—	—	—	$69.05^{+0.62}_{-0.63}$	$0.412^{+0.026}_{-0.032}$	50.19 ± 0.23	1.133 ± 0.085
Non-flat Λ CDM	GRB	$0.463^{+0.226}_{-0.084}$	$< 0.658^d$	$-0.007^{+0.251}_{-0.234}$	—	—	—	$0.412^{+0.026}_{-0.032}$	50.17 ± 0.28	1.121 ± 0.086
	H II G	$0.275^{+0.081}_{-0.078}$	$> 0.501^d$	$0.094^{+0.237}_{-0.163}$	—	—	$71.50^{+1.80}_{-1.81}$	—	—	—
	QSO-AS	$0.357^{+0.135}_{-0.135}$	—	$0.017^{+0.14}_{-0.277}$	—	—	$67.32^{+4.19}_{-5.44}$	—	—	—
	HQASG ^e	0.292 ± 0.044	$0.801^{+0.191}_{-0.055}$	$-0.093^{+0.092}_{-0.190}$	—	—	$71.33^{+1.75}_{-1.77}$	$0.413^{+0.026}_{-0.032}$	50.19 ± 0.24	1.130 ± 0.086
	$H(z)$ + BAO	0.309 ± 0.016	$0.636^{+0.081}_{-0.072}$	$0.055^{+0.082}_{-0.074}$	—	—	67.44 ± 2.33	—	—	—
	HzBHQSAG ^f	$0.311^{+0.012}_{-0.014}$	$0.708^{+0.053}_{-0.046}$	$-0.019^{+0.043}_{-0.048}$	—	—	69.72 ± 1.10	$0.412^{+0.026}_{-0.032}$	50.19 ± 0.23	1.132 ± 0.085
Flat XCDM	GRB	$> 0.366^d$	—	—	—	—	—	$0.411^{+0.025}_{-0.032}$	50.14 ± 0.28	1.119 ± 0.085
	H II G	$0.300^{+0.106}_{-0.083}$	—	—	$-1.180^{+0.560}_{-0.330}$	—	71.85 ± 1.96	—	—	—
	QSO-AS	$0.349^{+0.090}_{-0.143}$	—	—	$-1.161^{+0.430}_{-0.679}$	—	$68.39^{+6.14}_{-8.98}$	—	—	—
	HQASG ^e	$0.322^{+0.022}_{-0.044}$	—	—	$-1.379^{+0.613}_{-0.315}$	—	$72.00^{+1.99}_{-1.98}$	$0.412^{+0.026}_{-0.032}$	50.20 ± 0.24	1.130 ± 0.085
	$H(z)$ + BAO	$0.319^{+0.016}_{-0.017}$	—	—	$-0.888^{+0.098}_{-0.098}$	—	$66.26^{+2.32}_{-2.63}$	—	—	—
	HzBHQSAG ^f	$0.313^{+0.014}_{-0.015}$	—	—	$-1.050^{+0.090}_{-0.081}$	—	$69.85^{+1.42}_{-1.55}$	$0.412^{+0.026}_{-0.032}$	50.19 ± 0.24	1.134 ± 0.085
Non-flat XCDM	GRB	$> 0.386^d$	—	$0.121^{+0.464}_{-0.275}$	$> -1.218^d$	—	—	$0.411^{+0.026}_{-0.032}$	50.12 ± 0.28	1.122 ± 0.087
	H II G	$0.275^{+0.084}_{-0.125}$	—	$0.011^{+0.457}_{-0.460}$	$-1.125^{+0.537}_{-0.321}$	—	$71.71^{+2.07}_{-2.08}$	—	—	—
	QSO-AS	$0.359^{+0.111}_{-0.174}$	—	$0.115^{+0.466}_{-0.293}$	$-1.030^{+0.593}_{-0.548}$	—	$65.92^{+4.54}_{-9.54}$	—	—	—
	HQASG ^e	$0.303^{+0.073}_{-0.058}$	—	$-0.044^{+0.193}_{-0.217}$	$-1.273^{+0.501}_{-0.321}$	—	71.77 ± 2.02	$0.413^{+0.026}_{-0.031}$	50.20 ± 0.24	1.129 ± 0.085
	$H(z)$ + BAO	$0.323^{+0.021}_{-0.020}$	—	$-0.105^{+0.217}_{-0.162}$	$-0.818^{+0.212}_{-0.091}$	—	$66.20^{+2.29}_{-2.55}$	—	—	—
	HzBHQSAG ^f	0.310 ± 0.014	—	$-0.024^{+0.092}_{-0.093}$	$-1.019^{+0.202}_{-0.099}$	—	$69.63^{+1.45}_{-1.62}$	$0.412^{+0.026}_{-0.031}$	50.19 ± 0.23	1.132 ± 0.085
Flat ϕ CDM	GRB	$> 0.376^d$	—	—	—	—	—	$0.411^{+0.025}_{-0.032}$	50.13 ± 0.28	1.121 ± 0.087
	H II G	$0.210^{+0.043}_{-0.032}$	—	—	—	< 2.784	$71.23^{+1.79}_{-1.80}$	—	—	—
	QSO-AS	$0.329^{+0.086}_{-0.171}$	—	—	—	< 2.841	$64.42^{+4.47}_{-4.62}$	—	—	—
	HQASG ^e	$0.214^{+0.057}_{-0.061}$	—	—	—	< 2.584	70.30 ± 1.68	$0.413^{+0.026}_{-0.032}$	50.18 ± 0.24	1.142 ± 0.087
	$H(z)$ + BAO	$0.319^{+0.016}_{-0.017}$	—	—	—	$0.550^{+0.169}_{-0.494}$	$65.25^{+2.25}_{-1.82}$	—	—	—
	HzBHQSAG ^f	0.320 ± 0.013	—	—	—	< 0.418	$68.16^{+1.01}_{-0.80}$	$0.412^{+0.027}_{-0.033}$	50.20 ± 0.24	1.131 ± 0.088
Non-flat ϕ CDM	GRB	> 0.189	—	$0.251^{+0.247}_{-0.086}$	—	—	—	$0.411^{+0.026}_{-0.032}$	50.11 ± 0.28	1.128 ± 0.089
	H II G	< 0.321	—	$0.291^{+0.348}_{-0.113}$	—	< 4.590	$70.60^{+1.68}_{-1.84}$	—	—	—
	QSO-AS	$0.362^{+0.117}_{-0.103}$	—	$0.254^{+0.304}_{-0.092}$	—	< 4.752	$61.91^{+2.83}_{-4.92}$	—	—	—
	HQASG ^e	$0.205^{+0.044}_{-0.094}$	—	$-0.124^{+0.257}_{-0.253}$	—	< 3.414	70.66 ± 1.90	$0.414^{+0.027}_{-0.033}$	50.19 ± 0.24	1.134 ± 0.088
	$H(z)$ + BAO	0.321 ± 0.017	—	$-0.126^{+0.157}_{-0.130}$	—	$0.938^{+0.439}_{-0.644}$	65.93 ± 2.33	—	—	—
	HzBHQSAG ^f	0.313 ± 0.013	—	$-0.094^{+0.082}_{-0.064}$	—	< 0.905	68.79 ± 1.22	$0.412^{+0.027}_{-0.033}$	50.20 ± 0.24	1.126 ± 0.087

^c km s⁻¹ Mpc⁻¹.^d This is the 1σ limit. The 2σ limit is set by the prior, and is not shown here.^e H II G + QSO-AS + GRB.^f $H(z)$ + BAO + H II G + QSO-AS + GRB.

but do not rule out mild dark energy dynamics or a little spatial curvature energy density. More and better-quality higher- z GRB, H II G, QSO, and other data will significantly help to test these extensions of flat Λ CDM.

DATA AVAILABILITY

The H II G data used in this article were provided to us by the authors of [González-Morán et al. \(2019\)](#). These data will be shared on request to the corresponding author with the permission of the authors of [González-Morán et al. \(2019\)](#).

ACKNOWLEDGEMENTS

We thank Adam Riess for his comments and the anonymous referee for useful suggestions. This work was partially funded by Department of Energy grant DE-SC0011840. The computing for this project was performed on the Beowulf Research Cluster at Kansas State University, which is funded in part by NSF grants CNS-1006860, EPS-1006860, EPS-0919443, ACI-1440548, CHE-1726332, and NIH P20GM113109.

REFERENCES

- Agudelo Ruiz J. A., Fabris J. C., Velasquez-Toribio A. M., Shapiro I. L., 2020, preprint, ([arXiv:2007.12636](#))
- Alam S., et al., 2017, *MNRAS*, **470**, 2617
- Amati L., et al., 2002, *A&A*, **390**, 81
- Amati L., Guidorzi C., Frontera F., Della Valle M., Finelli F., Landi R., Montanari E., 2008, *MNRAS*, **391**, 577
- Amati L., Frontera F., Guidorzi C., 2009, *A&A*, **508**, 173
- Amati L., D'Agostino R., Luongo O., Muccino M., Tantalo M., 2019, *MNRAS*, **486**, L46
- Ata M., et al., 2018, *MNRAS*, **473**, 4773

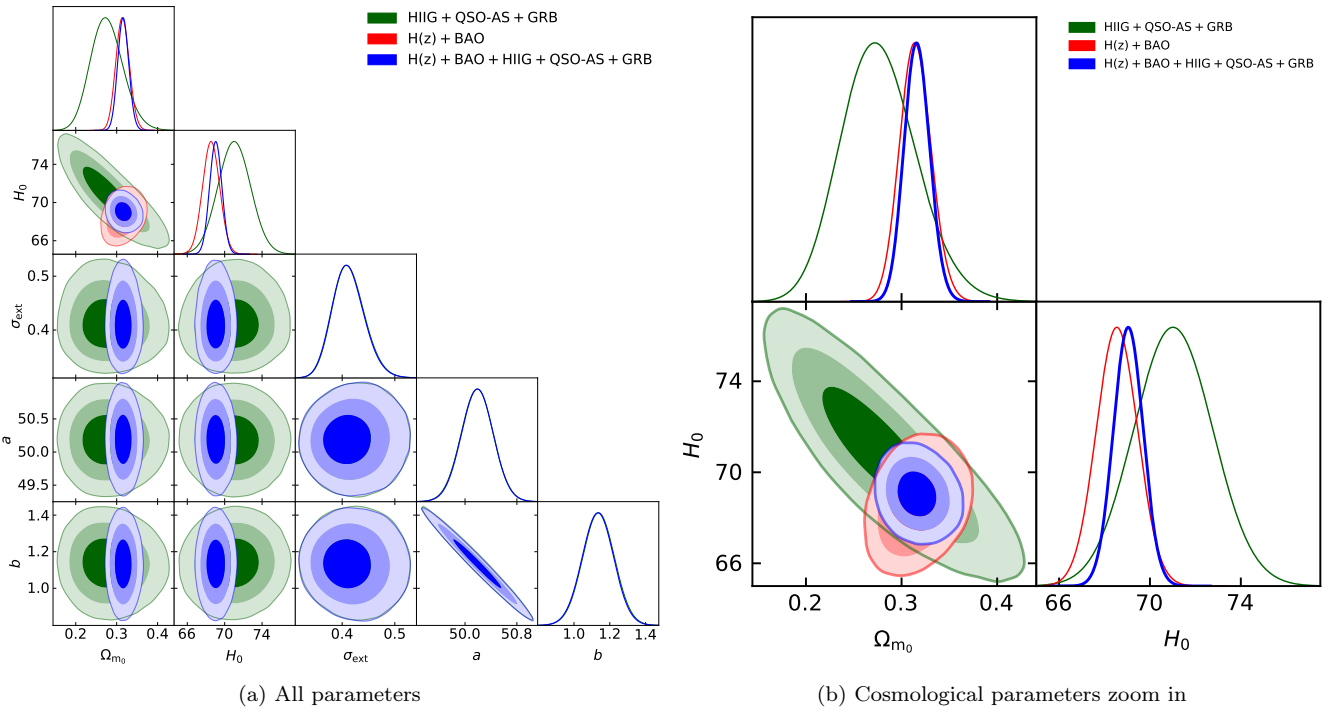


Figure 7. Same as Fig. 1 (flat Λ CDM) but for different combinations of data.

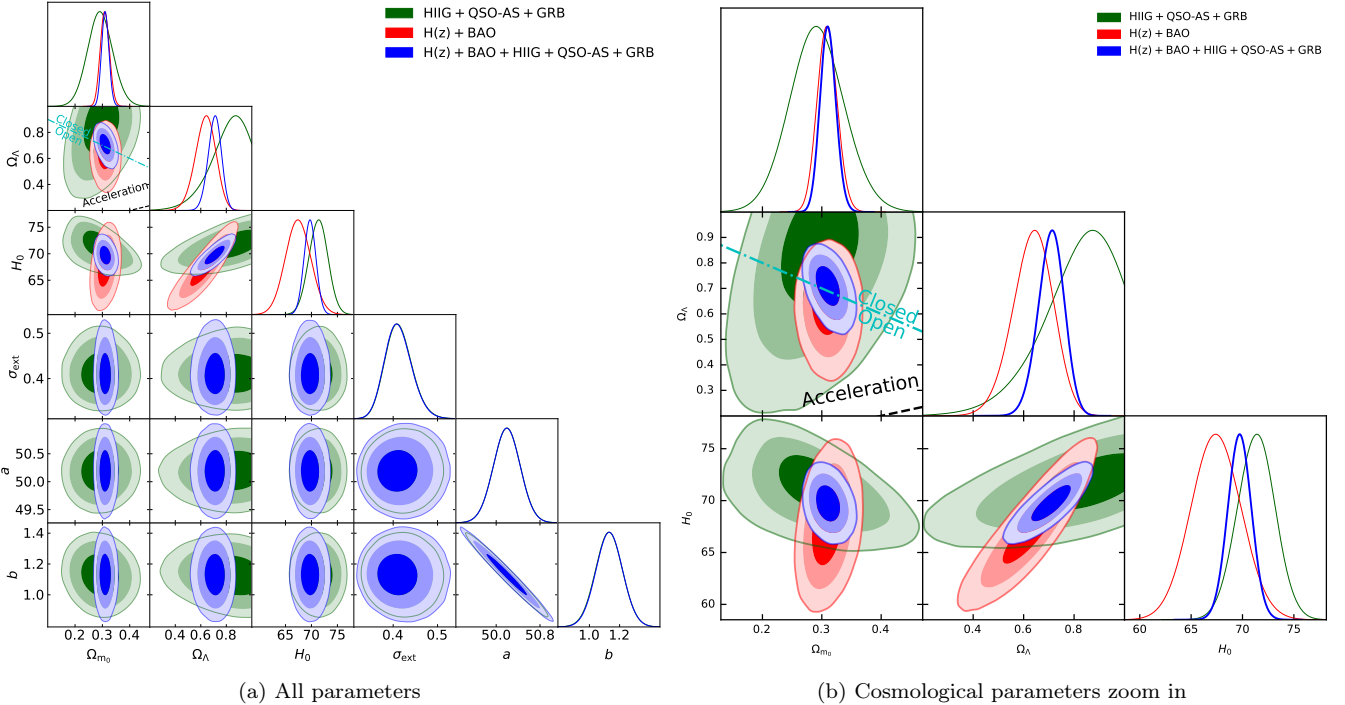


Figure 8. Same as Fig. 2 (non-flat Λ CDM) but for different combinations of data.

- Avsajanishvili O., Samushia L., Arkhipova N. A., Kahnashvili T., 2015, preprint, ([arXiv:1511.09317](https://arxiv.org/abs/1511.09317))
 Birrer S., et al., 2020, preprint, ([arXiv:2007.02941](https://arxiv.org/abs/2007.02941))
 Blum K., Castorina E., Simonović M., 2020, *ApJ*, **892**, L27
 Breuval L., et al., 2020, *A&A*, **643**, A115
 Campanelli L., Fogli G. L., Kahnashvili T., Marrone A., Ratra

- B., 2012, *European Physical Journal C*, **72**, 2218
 Cao S., Zheng X., Biesiada M., Qi J., Chen Y., Zhu Z.-H., 2017, *A&A*, **606**, A15
 Cao S., Ryan J., Ratra B., 2020, *MNRAS*, **497**, 3191
 Carter P., Beutler F., Percival W. J., Blake C., Koda J., Ross A. J., 2018, *MNRAS*, **481**, 2371

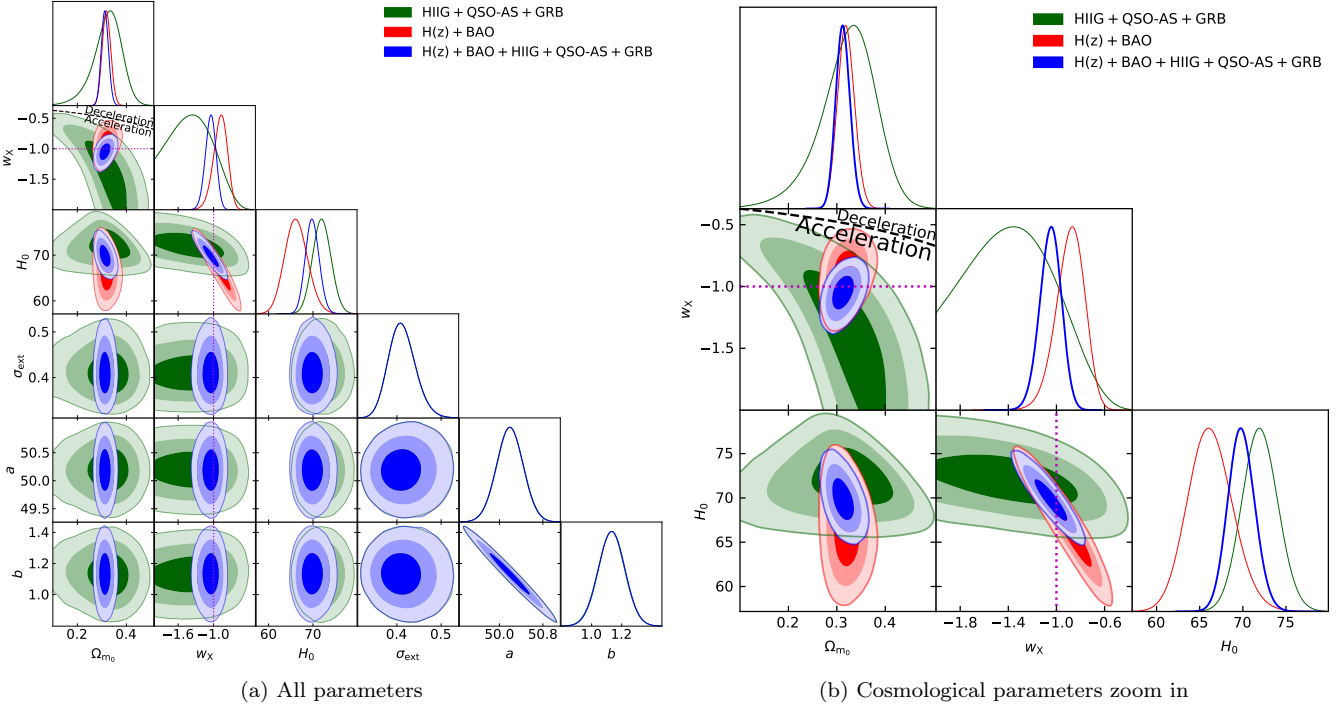


Figure 9. Same as Fig. 3 (flat XCDM) but for different combinations of data.

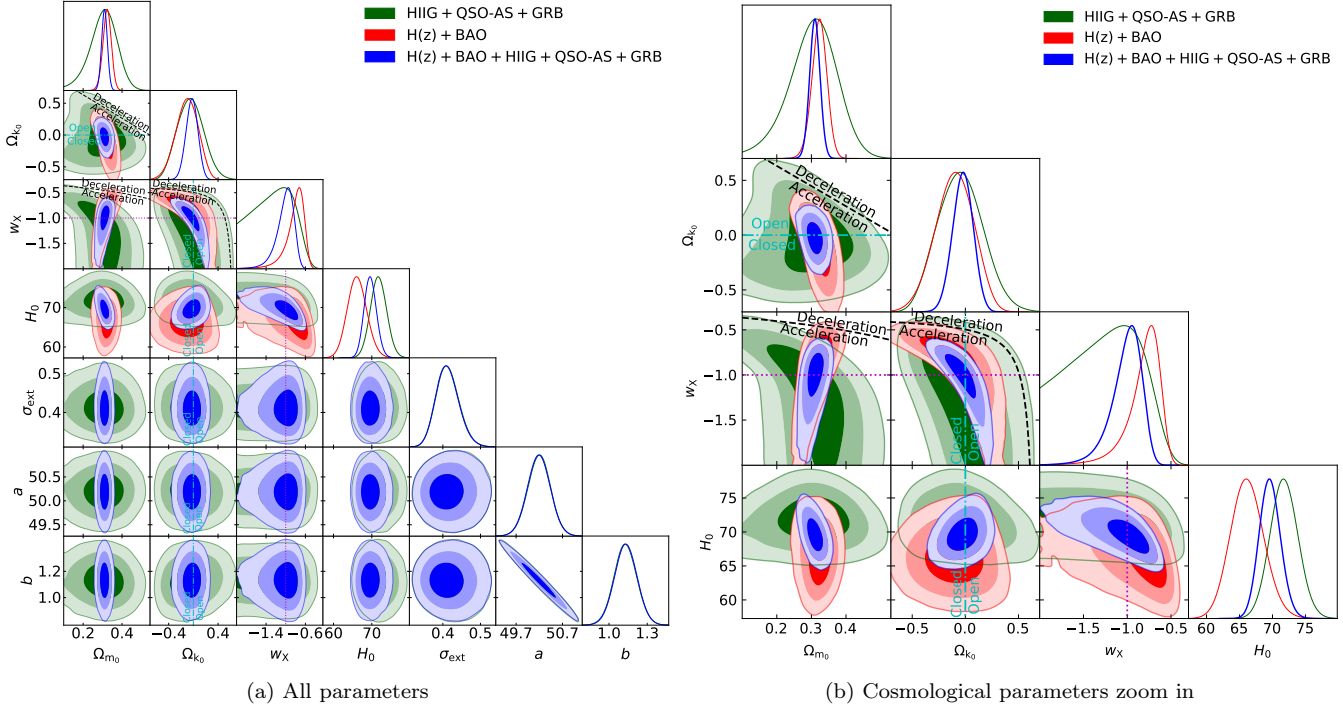
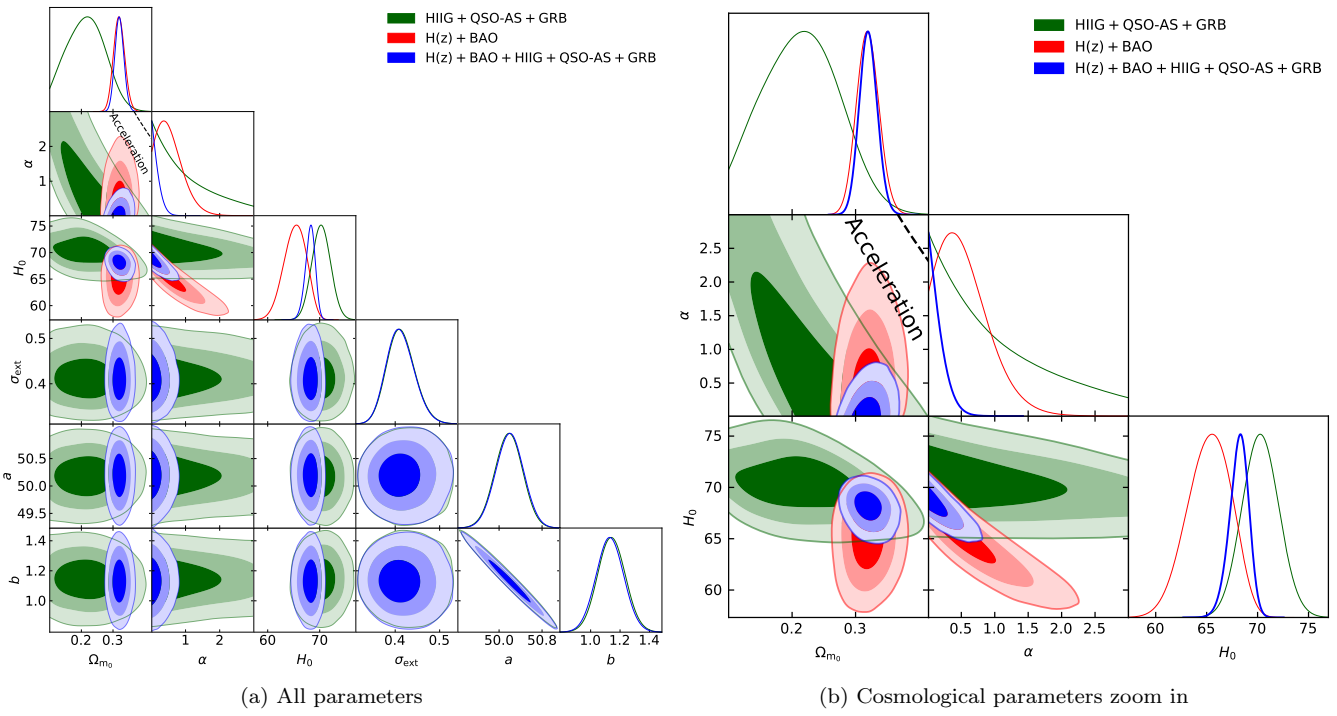
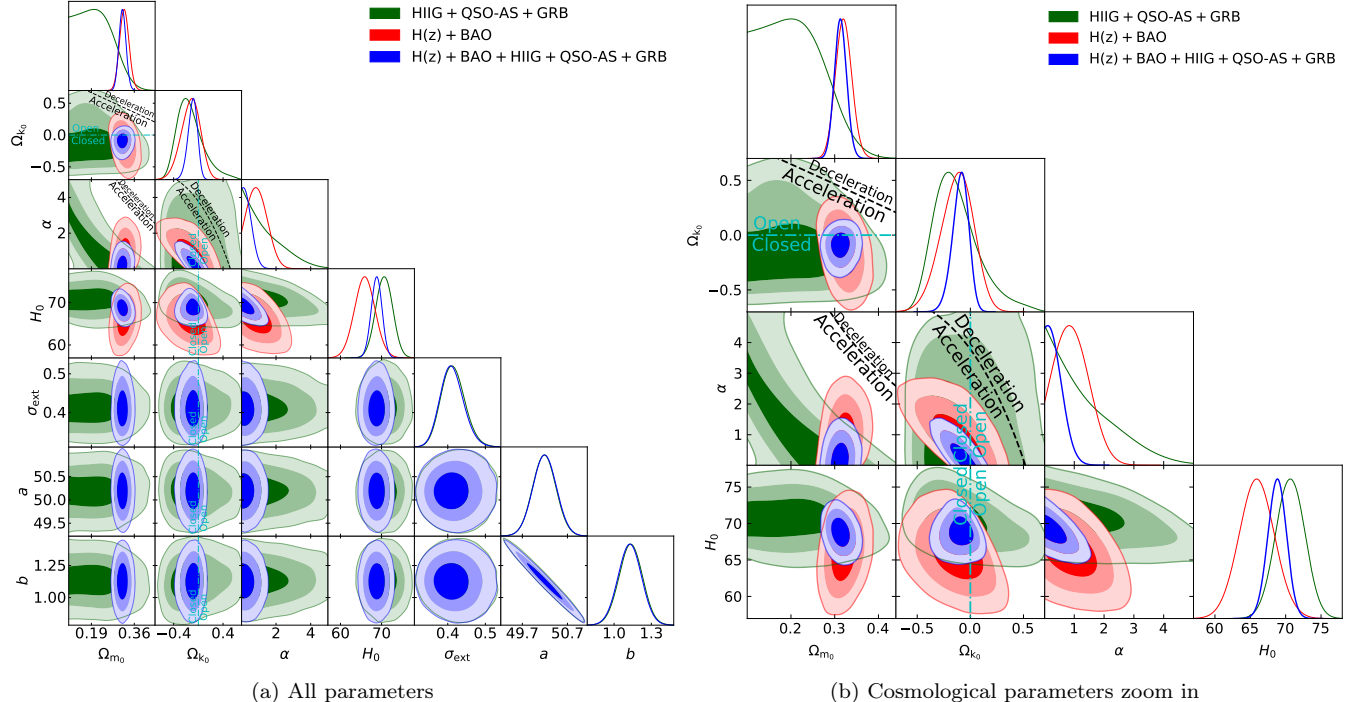


Figure 10. Same as Fig. 4 (non-flat XCDM) but for different combinations of data.

- Chávez R., Terlevich R., Terlevich E., Bresolin F., Melnick J., Plionis M., Basilakos S., 2014, *MNRAS*, **442**, 3565
 Chen G., Ratra B., 2003, *ApJ*, **582**, 586
 Chen G., Ratra B., 2004, *ApJ*, **612**, L1
 Chen G., Ratra B., 2011a, *PASP*, **123**, 1127
 Chen Y., Ratra B., 2011b, *Physics Letters B*, **703**, 406

- Chen G., Gott III J. R., Ratra B., 2003, *PASP*, **115**, 1269
 Chen Y., Ratra B., Biesiada M., Li S., Zhu Z.-H., 2016, *ApJ*, **829**, 61
 Chen Y., Kumar S., Ratra B., 2017, *ApJ*, **835**, 86
 Coley A. A., 2019, preprint, ([arXiv:1905.04588](https://arxiv.org/abs/1905.04588))
 Coley A. A., Ellis G. F. R., 2020, *Classical and Quantum Gravity*,

**Figure 11.** Same as Fig. 5 (flat ϕ CDM) but for different combinations of data.**Figure 12.** Same as Fig. 6 (non-flat ϕ CDM) but for different combinations of data.

- preprint, ([arXiv:1911.08228](#))
- Denzel P., Coles J. P., Saha P., Williams L. L. R., 2020, preprint, ([arXiv:2007.14398](#))
- Dhawan S., Jha S. W., Leibundgut B., 2018, *A&A*, **609**, A72
- Di Valentino E., Melchiorri A., Silk J., 2020, preprint, ([arXiv:2003.04935](#))
- Domínguez A., et al., 2019, *ApJ*, **885**, 137
- eBOSS Collaboration 2020, preprint, ([arXiv:2007.08991](#))
- Efstathiou G., 2020, preprint, ([arXiv:2007.10716](#))
- Efstathiou G., Gratton S., 2020, *MNRAS*, **496**, L91
- Fana Dirisra F., et al., 2019, *ApJ*, **887**, 13
- Farooq O., Ratra B., 2013, *ApJ*, **766**, L7
- Farooq O., Crandall S., Ratra B., 2013, *Physics Letters B*, **726**, 72
- Farooq O., Mania D., Ratra B., 2015, *Ap&SS*, **357**, 11
- Farooq O., Ranjeet Madiyar F., Crandall S., Ratra B., 2017, *ApJ*, **835**, 26
- Fernández Arenas D., et al., 2018, *MNRAS*, **474**, 1250
- Foreman-Mackey D., Hogg D. W., Lang D., Goodman J., 2013, *PASP*, **125**, 306
- Freedman W. L., et al., 2019, *ApJ*, **882**, 34
- Freedman W. L., et al., 2020, *ApJ*, **891**, 57
- Gao C., Chen Y., Zheng J., 2020, *Research in Astronomy and Astrophysics*, **20**, 151
- Geng C.-Q., Hsu Y.-T., Yin L., Zhang K., 2020, *Chinese Physics C*, **44**, 105104
- Ghirlanda G., Ghisellini G., Lazzati D., 2004, *ApJ*, **616**, 331
- Gómez-Valet A., Amendola L., 2018, *J. Cosmology Astropart. Phys.*, **4**, 051
- González-Morán A. L., et al., 2019, *MNRAS*, **487**, 4669
- Gott III J. R., Vogeley M. S., Podariu S., Ratra B., 2001, *ApJ*, **549**, 1
- Gurvits L. I., Kellermann K. I., Frey S., 1999, *A&A*, **342**, 378
- Handley W., 2019, *Phys. Rev. D*, **100**, 123517
- Hogg D. W., 1999, preprint, ([arXiv:astro-ph/9905116](#))
- Jesus J. F., Valentim R., Moraes P. H. R. S., Malheiro M., 2020, *MNRAS*,
- Jones D. H., et al., 2009, *MNRAS*, **399**, 683
- Khadka N., Ratra B., 2020a, *MNRAS*, **492**, 4456
- Khadka N., Ratra B., 2020b, *MNRAS*, **497**, 263
- Khadka N., Ratra B., 2020c, *MNRAS*, **499**, 391
- Khetan N., et al., 2020, preprint, ([arXiv:2008.07754](#))
- Kumar D., Jain D., Mahajan S., Mukherjee A., Rani N., 2020, preprint, ([arXiv:2002.06354](#))
- Lamb D. Q., Reichart D. E., 2000, *ApJ*, **536**, 1
- Lamb D. Q., Reichart D. E., 2001, in Costa E., Frontera F., Hjorth J., eds, Gamma-ray Bursts in the Afterglow Era. p. 226 ([arXiv:astro-ph/0108099](#)), doi:10.1007/10853853_61
- Lewis A., 2019, preprint, ([arXiv:1910.13970](#))
- Li E.-K., Du M., Xu L., 2020, *MNRAS*, **491**, 4960
- Liang E., Zhang B., 2005, *ApJ*, **633**, 611
- Lima J. A. S., Alcaniz J. S., 2002, *ApJ*, **566**, 15
- Lin W., Ishak M., 2019, preprint, ([arXiv:1909.10991](#))
- Liu J., Wei H., 2015, *General Relativity and Gravitation*, **47**, 141
- Lyu M.-Z., Haridasu B. S., Viel M., Xia J.-Q., 2020, *ApJ*, **900**, 160
- Mania D., Ratra B., 2012, *Physics Letters B*, **715**, 9
- Martin J., 2012, *Comptes Rendus Physique*, **13**, 566
- Martinelli M., Tutzus I., 2019, *Symmetry*, **11**, 986
- Moresco M., et al., 2012, *J. Cosmology Astropart. Phys.*, **8**, 006
- Moresco M., et al., 2016, *J. Cosmology Astropart. Phys.*, **5**, 014
- Moresco M., Jimenez R., Verde L., Pozzetti L., Cimatti A., Citro A., 2018, *ApJ*, **868**, 84
- Moresco M., Jimenez R., Verde L., Cimatti A., Pozzetti L., 2020, *ApJ*, **898**, 82
- Muccino M., 2020, *Symmetry*, **12**, 1118
- Ooba J., Ratra B., Sugiyama N., 2018a, *ApJ*, **864**, 80
- Ooba J., Ratra B., Sugiyama N., 2018b, *ApJ*, **866**, 68
- Ooba J., Ratra B., Sugiyama N., 2018c, *ApJ*, **869**, 34
- Ooba J., Ratra B., Sugiyama N., 2019, *Ap&SS*, **364**, 176
- Park C.-G., Ratra B., 2018, *ApJ*, **868**, 83
- Park C.-G., Ratra B., 2019a, *Ap&SS*, **364**, 82
- Park C.-G., Ratra B., 2019b, *Ap&SS*, **364**, 134
- Park C.-G., Ratra B., 2019c, *ApJ*, **882**, 158
- Park C.-G., Ratra B., 2020, *Phys. Rev. D*, **101**, 083508
- Pavlov A., Westmoreland S., Saaidi K., Ratra B., 2013, *Phys. Rev. D*, **88**, 123513
- Peebles P. J. E., 1984, *ApJ*, **284**, 439
- Peebles P. J. E., Ratra B., 1988, *ApJ*, **325**, L17
- Philcox O. H. E., Ivanov M. M., Simonović M., Zaldarriaga M., 2020, *J. Cosmology Astropart. Phys.*, **2020**, 032
- Planck Collaboration 2020, *A&A*, **641**, A6
- Plionis M., Terlevich R., Basilakos S., Bresolin F., Terlevich E., Melnick J., Georganopoulos I., 2009, in *Journal of Physics Conference Series*. p. 012032 ([arXiv:0903.0131](#)), doi:10.1088/1742-6596/189/1/012032
- Rameez M., Sarkar S., 2019, preprint, ([arXiv:1911.06456](#))
- Rana A., Jain D., Mahajan S., Mukherjee A., 2017, *J. Cosmology Astropart. Phys.*, **3**, 028
- Ratra B., Peebles P. J. E., 1988, *Phys. Rev. D*, **37**, 3406
- Ratra B., Vogeley M. S., 2008, *PASP*, **120**, 235
- Riess A. G., 2019, *Nature Reviews Physics*, **2**, 10
- Riess A. G., Casertano S., Yuan W., Macri L. M., Scolnic D., 2019, *ApJ*, **876**, 85
- Rigault M., et al., 2015, *ApJ*, **802**, 20
- Risaliti G., Lusso E., 2015, *ApJ*, **815**, 33
- Risaliti G., Lusso E., 2019, *Nature Astronomy*, **3**, 272
- Ross A. J., Samushia L., Howlett C., Percival W. J., Burden A., Manera M., 2015, *MNRAS*, **449**, 835
- Ryan J., Doshi S., Ratra B., 2018, *MNRAS*, **480**, 759
- Ryan J., Chen Y., Ratra B., 2019, *MNRAS*, **488**, 3844
- Samushia L., Ratra B., 2010, *ApJ*, **714**, 1347
- Samushia L., Chen G., Ratra B., 2007, preprint, ([arXiv:0706.1963](#))
- Samushia L., Dev A., Jain D., Ratra B., 2010, *Physics Letters B*, **693**, 509
- Sangwan A., Tripathi A., Jassal H. K., 2018, preprint, ([arXiv:1804.09350](#))
- Schöneberg N., Lesgourgues J., Hooper D. C., 2019, *J. Cosmology Astropart. Phys.*, **2019**, 029
- Scolnic D. M., et al., 2018, *ApJ*, **859**, 101
- Shirokov S. I., Sokolov I. V., Lovyagin N. Y., Amati L., Baryshev Y. V., Sokolov V. V., Gorokhov V. L., 2020, *MNRAS*, **496**, 1530
- Siegel E. R., Guzmán R., Gallego J. P., Orduña López M., Rodríguez Hidalgo P., 2005, *MNRAS*, **356**, 1117
- Singh A., Sangwan A., Jassal H. K., 2019, *J. Cosmology Astropart. Phys.*, **2019**, 047
- Solà Peracaula J., de Cruz Pérez J., Gómez-Valet A., 2018, *MNRAS*, **478**, 4357
- Solà Peracaula J., Gómez-Valet A., de Cruz Pérez J., 2019, *Physics of the Dark Universe*, **25**, 100311
- Solà J., Gómez-Valet A., de Cruz Pérez J., 2017, *Modern Physics Letters A*, **32**, 1750054
- Terlevich R., Terlevich E., Melnick J., Chávez R., Plionis M., Bresolin F., Basilakos S., 2015, *MNRAS*, **451**, 3001
- Ureña-López L. A., Roy N., 2020, *Phys. Rev. D*, **102**, 063510
- Velásquez-Toribio A. M., Fabris J. C., 2020, preprint, ([arXiv:2008.12741](#))
- Vishwakarma R. G., 2001, *Classical and Quantum Gravity*, **18**, 1159
- Wang F. Y., Dai Z. G., Liang E. W., 2015, *New Astron. Rev.*, **67**, 1
- Wang J. S., Wang F. Y., Cheng K. S., Dai Z. G., 2016, *A&A*, **585**, A68
- Wei J.-J., 2018, *ApJ*, **868**, 29

- Wei J.-J., Melia F., 2020, *ApJ*, **888**, 99
 Yang Y., Gong Y., 2020, preprint, ([arXiv:2007.05714](#))
 Yang T., Banerjee A., Colgáin E. Ó., 2019, preprint, ([arXiv:1911.01681](#))
 Yashar M., Bozek B., Abrahamse A., Albrecht A., Barnard M., 2009, *Phys. Rev. D*, **79**, 103004
 Yu H., Wang F. Y., 2016, *ApJ*, **828**, 85
 Yu H., Ratra B., Wang F.-Y., 2018, *ApJ*, **856**, 3
 Zeng H., Yan D., 2019, *ApJ*, **882**, 87
 Zhai Z., Blanton M., Slosar A., Tinker J., 2017, *ApJ*, **850**, 183
 Zhai Z., Park C.-G., Wang Y., Ratra B., 2020, *J. Cosmology Astropart. Phys.*, **2020**, 009
 Zhang J., 2018, *PASP*, **130**, 084502
 Zhang X., Huang Q.-G., 2020, preprint, ([arXiv:2006.16692](#))
 Zhang B. R., Childress M. J., Davis T. M., Karpenka N. V., Lidman C., Schmidt B. P., Smith M., 2017, *MNRAS*, **471**, 2254
 Zhu Z.-H., Fujimoto M.-K., 2002, *ApJ*, **581**, 1

APPENDIX A: QSO-FLUX

QSOs obey a nonlinear relation between their luminosities in the X-ray and UV bands. Using a sample of 808 QSOs in the redshift range $0.061 \leq z \leq 6.280$, [Risaliti & Lusso \(2015\)](#) confirmed that this relation can be written

$$\log L_X = \beta + \gamma \log L_{UV}, \quad (\text{A1})$$

where L_X and L_{UV} are the X-ray and UV luminosities of the QSOs. To make contact with observations, equation (A1) must be expressed in terms of the fluxes F_X and F_{UV} measured at fixed rest-frame wavelengths in the X-ray and UV bands, respectively. With this, equation (A1) becomes

$$\log F_X = \beta + (\gamma - 1) \log 4\pi + \gamma \log F_{UV} + 2(\gamma - 1) \log D_L. \quad (\text{A2})$$

Here D_L (defined in equation 9) is the luminosity distance, which depends on the parameters of our cosmological models. We also treat the slope γ and intercept β as free parameters in our cosmological model fits.

For QSO-Flux data, the natural log of its likelihood function is

$$\ln \mathcal{L}_{\text{QF}} = -\frac{1}{2} \sum_{i=1}^N \left[\frac{[\log(F_X^{\text{obs}})_i - \log(F_X^{\text{th}})_i]^2}{s_i^2} + \ln(2\pi s_i^2) \right],$$

where $s_i^2 = \sigma_i^2 + \delta^2$. Here σ_i is the uncertainty in $\log(F_X^{\text{obs}})_i$, and δ is the global intrinsic dispersion in the data (including the systematic uncertainties), which we treat as a free parameter in our cosmological model fits. We use the [Risaliti & Lusso \(2019\)](#) compilation of 1598 QSO-Flux measurements in the range $0.036 \leq z \leq 5.1003$. The flat priors of cosmological parameters and the Amati relation parameters are in Sec. 4 and, as in [Khadka & Ratra \(2020b\)](#), the flat priors of the parameters δ , γ , and β are non-zero over $0 \leq \delta \leq e^{10}$, $-2 \leq \gamma \leq 2$, and $0 \leq \beta \leq 11$, respectively.

As discussed in [Khadka & Ratra \(2020b\)](#) the QSO-Flux data alone favors large Ω_{m0} values for the physically-motivated flat and non-flat ΛCDM and ϕCDM models. [Risaliti & Lusso \(2019\)](#) and [Khadka & Ratra \(2020b\)](#) note that this is largely a consequence of the $z \sim 2\text{--}5$ QSO data. While these large Ω_{m0} values differ from almost all other measurements of Ω_{m0} , the QSO-Flux data have larger error bars and their cosmological constraint contours are not in

conflict with those from other data sets. For these reasons we have used the QSO-Flux data, but in this Appendix and not in the main text, and we have not computed QSO-Flux data results for the ϕCDM cases (these being computationally demanding). We briefly summarize our constraints, listed in Tables A1 and A2 and shown in Figs. A1–A4, below.

A1 QSO-Flux constraints

Except for flat ΛCDM , the constraints on Ω_{m0} in the QSO-Flux only case are 2σ larger than those in the combined HzBHQASQFG case (see Sec. A3). QSO-Flux data cannot constrain α , nor can they constrain H_0 (for the same reason that GRB data cannot constrain this parameter; see Section 5.1). QSO-Flux data set upper limits on w_X for flat and non-flat XCDM, with $w_X = -1$ within the 1σ range.

A2 $\text{H}_{\text{II}}\text{G}$, QSO-AS, QSO-Flux, and GRB (HQASQFG) constraints

When adding QSO-Flux to HQASG data, the joint constraints favor larger Ω_{m0} and lower Ω_{k0} . In non-flat ΛCDM closed geometry is favored at 3.24σ . The H_0 constraints are only mildly affected by the addition of the QSO-Flux data. The constraint on w_X changes from $-1.379^{+0.361}_{-0.375}$ in the HQASG case to < -1.100 (2σ limit) in the HQASQFG case for flat XCDM, while for non-flat XCDM, the constraint on w_X in the HQASQFG case is 0.40σ lower than that in the HQASG case and is 1.80σ away from $w_X = -1$.

A3 $H(z)$, BAO, $\text{H}_{\text{II}}\text{G}$, QSO-AS, QSO-Flux, and GRB (HzBHQASQFG) constraints

When adding QSO-Flux to the HzBHQASG combination, the Ω_{m0} central values are only slightly larger because the $H(z) + \text{BAO}$ data dominate this compilation. The joint-constraint central Ω_{k0} values are lower, and consistent with flat geometry, while the constraints on H_0 from this combination are almost unaltered. The constraints on w_X are 0.02σ lower and 0.23σ higher for flat and non-flat XCDM, respectively, both being consistent with $w_X = -1$ within 1σ .

A4 Model comparison

From Table A1, we see that the reduced χ^2 of the QSO-Flux case for all models is near unity (~ 1.01) and that the reduced χ^2 of cases that include QSO-Flux is brought down to $\sim 1.24\text{--}1.26$ for all models. Based on the *BIC* (see Table A1), flat ΛCDM is the most favored model, while based on the *AIC*, non-flat XCDM, flat XCDM, and flat ΛCDM are the most favored models for the QSO-Flux, HQASQFG, and HzBHQASQFG combinations, respectively.¹⁵ From ΔAIC and ΔBIC , we find mostly weak or positive evidence against the models, and only in a few cases do we find strong evidence against our models. According to ΔBIC , the evidence against non-flat XCDM is strong for the QSO-Flux data, and very strong for the HQASQFG and HzBHQASQFG

¹⁵ Note that based on the $\Delta\chi^2$ results of Table A1 flat ΛCDM has the minimum χ^2 in the QSO-Flux, HQASQFG, and HzBHQASQFG cases.

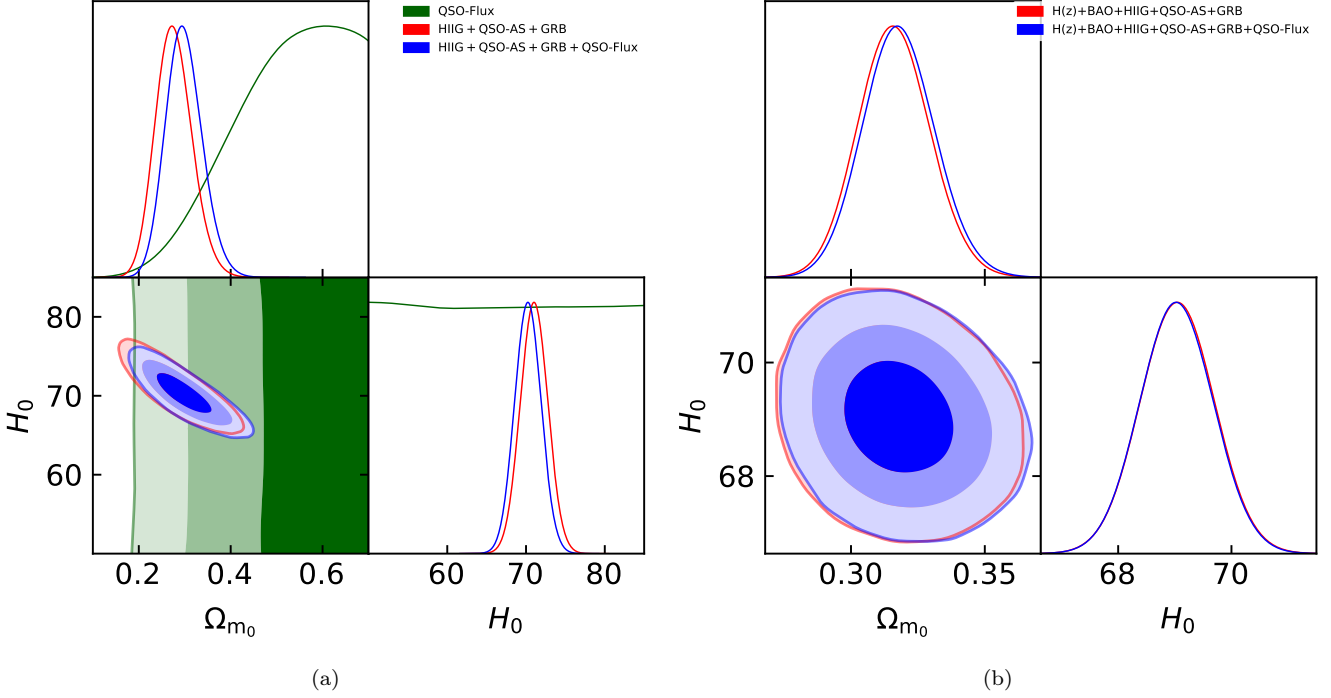


Figure A1. Same as Fig. 1 (flat Λ CDM) but for different combinations of data and showing only cosmological parameters.

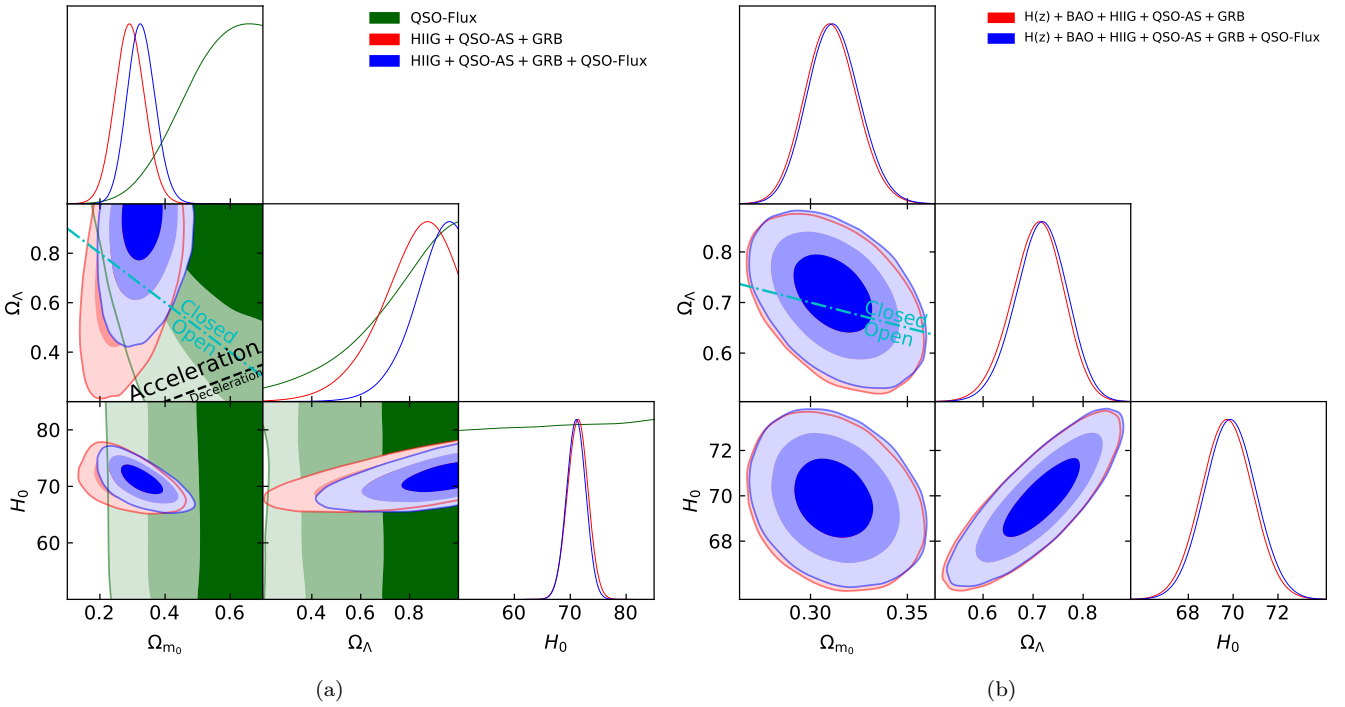


Figure A2. Same as Fig. 2 (non-flat Λ CDM) but for different combinations of data and showing only cosmological parameters.

data, and the evidence against non-flat Λ CDM is strong for the HzHQASQFG data. According to ΔAIC , the evidence against flat XCDM is strong for the HzHQASQFG data.

This paper has been typeset from a $\text{\TeX}/\text{\LaTeX}$ file prepared by the author.

Table A1: Unmarginalized best-fitting parameter values for all models from various combinations of data.

Model	Data set	Ω_{m_0}	Ω_Λ	Ω_{k_0}	w_{X}	α	H_0^{c}	σ_{ext}	a	b	δ	γ	β	χ^2	ν	$-2 \ln \mathcal{L}_{\max}$	AIC	BIC	ΔAIC	ΔBIC
Flat Λ CDM	QSO-Flux	0.315	0.685	—	—	—	68.69	—	—	—	—	—	—	1603.28	1593	-50.13	-13.24	0.00	1.62	0.00
	HQASG ^d	0.271	0.729	—	—	—	71.13	0.407	50.18	1.138	—	—	—	879.42	387	895.05	905.05	924.91	0.12	0.00
	HQASQFG ^e	0.305	0.695	—	—	—	70.01	0.399	50.20	1.132	0.231	0.639	7.083	2480.01	1982	848.53	864.53	909.29	0.00	2.58
	HzBHQASGF ^f	0.317	0.683	—	—	—	69.06	0.404	50.19	1.134	—	—	—	903.61	429	917.79	948.16	1.52	0.00	0.00
	HzBHQASQFG ^g	0.317	0.683	—	—	—	69.06	0.399	50.23	1.119	0.232	0.637	7.144	2499.87	2024	870.31	886.31	931.25	0.00	0.00
Non-flat Λ CDM	QSO-Flux	0.540	0.985	-0.525	—	—	75.75	—	—	—	0.230	0.611	7.888	1603.83	1592	-53.25	-41.25	-8.99	0.55	0.50
	HQASG ^d	0.291	0.876	-0.167	—	—	72.00	0.406	50.22	1.120	—	—	—	879.30	386	894.02	906.02	929.85	0.00	0.97
	HQASQFG ^e	0.325	0.944	-0.269	—	—	71.49	0.404	50.21	1.116	0.230	0.632	7.304	2486.97	1981	844.38	862.38	912.75	6.96	0.43
	HzBHQASGF ^f	0.309	0.716	-0.025	—	—	69.77	0.402	50.17	1.141	—	—	—	904.47	428	917.17	929.17	953.61	2.38	3.46
	HzBHQASQFG ^g	0.309	0.709	-0.018	—	—	69.59	0.412	50.21	1.128	0.231	0.637	7.151	2503.43	2023	869.71	887.71	938.26	3.56	5.45
																			7.01	
Flat XCDM	QSO-Flux	0.477	—	—	-1.988	—	60.86	—	—	—	0.230	0.625	7.530	1604.18	1592	-52.13	-40.13	-7.88	0.90	1.62
	HQASG ^d	0.320	—	—	-1.306	—	72.03	0.404	50.20	1.131	—	—	—	880.47	386	894.27	906.27	930.10	1.17	1.22
	HQASQFG ^e	0.370	—	—	-1.980	—	73.66	0.399	50.18	1.129	0.231	0.632	7.301	2485.59	1981	843.95	861.95	912.31	5.58	0.00
	HzBHQASGF ^f	0.313	—	—	-1.052	—	69.90	0.407	50.19	1.132	—	—	—	902.09	428	917.55	929.55	953.99	0.00	1.76
	HzBHQASQFG ^g	0.313	—	—	-1.046	—	69.84	0.401	50.18	1.134	0.231	0.635	7.215	2506.25	2023	870.16	888.16	938.71	6.38	5.83
																			7.46	
Non-flat XCDM	QSO-Flux	0.507	—	-0.376	-1.996	—	75.28	—	—	—	0.229	0.611	7.934	1614.59	1591	-55.75	-41.75	-4.12	11.31	0.00
	HQASG ^d	0.300	—	-0.161	-1.027	—	80.36	0.405	50.21	1.122	—	—	—	879.48	385	894.01	908.01	935.81	0.18	2.96
	HQASQFG ^e	0.395	—	-0.138	-1.639	—	73.48	0.411	50.21	1.112	0.230	0.627	7.441	2486.77	1980	843.65	863.65	919.61	6.76	10.90
	HzBHQASGF ^f	0.312	—	-0.045	-0.959	—	69.46	0.402	50.23	1.117	—	—	—	904.17	427	917.07	931.07	959.58	2.08	10.32
	HzBHQASQFG ^g	0.316	—	-0.089	-0.891	—	69.05	0.410	50.23	1.111	0.230	0.633	7.247	2516.49	2022	869.25	889.25	945.41	16.62	11.42

^c km s⁻¹ Mpc⁻¹.^d H₁IG + QSO-AS + GRB.^e H₁IG + QSO-AS + GRB + QSO-Flux.^f $H(z)$ + BAO + H₁nG + QSO-AS + GRB.^g $H(z)$ + BAO + H₁nG + QSO-AS + GRB + QSO-Flux.

Table A2: One-dimensional marginalized best-fitting parameter values and uncertainties ($\pm 1\sigma$ error bars or 2σ limits) for all models from various combinations of data.

Model	Data set	Ω_{m0}	Ω_Λ	Ω_{k_0}	w_X	α	H_0^c	σ_{ext}	a	b	δ	γ	β
Flat Λ CDM	QSO-Flux	> 0.313	—	—	—	—	—	—	0.231 ± 0.004	0.626 ± 0.011	7.469 ± 0.321	—	—
	HQASG ^d	$0.277^{+0.034}_{-0.041}$	—	—	—	-71.03 ± 1.67	$0.413^{+0.026}_{-0.032}$	50.19 ± 0.24	1.138 ± 0.085	—	—	—	—
	HQASQFG ^e	$0.299^{+0.036}_{-0.043}$	—	—	—	$-70.25^{+1.60}_{-1.61}$	$0.412^{+0.027}_{-0.032}$	50.18 ± 0.24	1.136 ± 0.085	$0.231^{+0.005}_{-0.004}$	$0.639^{+0.009}_{-0.010}$	$7.091^{+0.281}_{-0.279}$	—
	HzBHQASG ^f	0.316 ± 0.013	—	—	—	$-69.05^{+0.62}_{-0.63}$	$0.412^{+0.026}_{-0.032}$	50.19 ± 0.23	1.133 ± 0.085	—	—	—	—
	HzBHQASQFG ^g	0.318 ± 0.013	—	—	—	-69.03 ± 0.62	$0.412^{+0.026}_{-0.032}$	50.19 ± 0.23	1.133 ± 0.084	0.231 ± 0.004	0.637 ± 0.009	7.146 ± 0.268	—
	QSO-Flux	> 0.353	> 0.357	$-0.303^{+0.131}_{-0.092}$	—	—	—	—	—	—	—	$0.231^{+0.004}_{-0.005}$	0.618 ± 0.012
Non-flat Λ CDM	HQASG ^d	0.292 ± 0.044	$0.801^{+0.191}_{-0.055}$	$-0.093^{+0.252}_{-0.092}$	—	$-71.33^{+1.75}_{-1.77}$	$0.413^{+0.026}_{-0.032}$	50.19 ± 0.24	1.130 ± 0.086	—	—	—	—
	HQASQFG ^e	$0.327^{+0.039}_{-0.043}$	> 0.691	$-0.294^{+0.063}_{-0.190}$	—	-71.07 ± 1.64	$0.413^{+0.027}_{-0.032}$	50.20 ± 0.24	1.120 ± 0.086	0.231 ± 0.004	0.632 ± 0.010	$7.291^{+0.346}_{-0.305}$	—
	HzBHQASG ^f	$0.311^{+0.012}_{-0.013}$	$0.708^{+0.053}_{-0.053}$	$-0.019^{+0.125}_{-0.043}$	—	-69.72 ± 1.10	$0.412^{+0.026}_{-0.032}$	50.19 ± 0.23	1.132 ± 0.085	—	—	—	—
	HzBHQASQFG ^g	$0.312^{+0.012}_{-0.013}$	$0.716^{+0.056}_{-0.052}$	-0.028 ± 0.045	—	-69.88 ± 1.10	$0.412^{+0.026}_{-0.032}$	50.19 ± 0.23	1.131 ± 0.084	0.231 ± 0.004	0.637 ± 0.009	7.144 ± 0.270	—
	QSO-Flux	$0.496^{+0.192}_{-0.069}$	—	—	$< -1.042^{\text{h}}$	—	—	—	—	0.231 ± 0.004	0.624 ± 0.011	7.508 ± 0.326	—
	HQASG ^d	$0.322^{+0.062}_{-0.040}$	—	—	$-1.379^{+0.361}_{-0.375}$	$-72.00^{+1.99}_{-1.98}$	$0.412^{+0.026}_{-0.032}$	50.20 ± 0.24	1.130 ± 0.085	—	—	—	—
Flat XCDM	HQASQFG ^e	$0.358^{+0.040}_{-0.038}$	—	—	< -1.100	-72.14 ± 1.91	$0.411^{+0.026}_{-0.032}$	50.20 ± 0.23	1.125 ± 0.084	0.231 ± 0.004	$0.633^{+0.009}_{-0.010}$	$7.268^{+0.287}_{-0.288}$	—
	HzBHQASG ^f	$0.313^{+0.014}_{-0.014}$	—	—	$-1.050^{+0.090}_{-0.081}$	$-69.85^{+1.42}_{-1.55}$	$0.412^{+0.026}_{-0.032}$	50.19 ± 0.24	1.134 ± 0.085	—	—	—	—
	HzBHQASQFG ^g	$0.315^{+0.015}_{-0.015}$	—	—	$-1.052^{+0.091}_{-0.081}$	-69.85 ± 1.48	$0.413^{+0.026}_{-0.032}$	50.19 ± 0.24	1.133 ± 0.086	0.231 ± 0.004	0.637 ± 0.009	$7.135^{+0.270}_{-0.271}$	—
	QSO-Flux	$0.515^{+0.184}_{-0.050}$	—	$-0.310^{+0.137}_{-0.050}$	< -0.294	—	—	—	—	0.231 ± 0.004	0.624 ± 0.011	7.508 ± 0.326	—
	HQASG ^d	$0.303^{+0.073}_{-0.058}$	—	$-0.044^{+0.183}_{-0.177}$	$-1.273^{+0.501}_{-0.321}$	-71.77 ± 2.02	$0.413^{+0.026}_{-0.032}$	50.20 ± 0.24	1.129 ± 0.085	—	$0.231^{+0.004}_{-0.005}$	0.615 ± 0.013	$7.817^{+0.398}_{-0.400}$
	HQASQFG ^e	$0.367^{+0.048}_{-0.048}$	—	$-0.146^{+0.143}_{-0.147}$	$-1.433^{+0.241}_{-0.493}$	$-72.27^{+2.01}_{-1.99}$	$0.413^{+0.026}_{-0.032}$	50.21 ± 0.24	1.116 ± 0.085	0.231 ± 0.004	$0.629^{+0.011}_{-0.010}$	7.382 ± 0.321	—
Non-flat XCDM	HzBHQASG ^f	0.310 ± 0.014	—	$-0.024^{+0.092}_{-0.093}$	$-1.019^{+0.092}_{-0.093}$	$-69.63^{+1.45}_{-1.62}$	$0.412^{+0.026}_{-0.031}$	50.19 ± 0.23	1.132 ± 0.085	—	—	—	—
	HzBHQASQFG ^g	$0.314^{+0.014}_{-0.015}$	—	$-0.060^{+0.096}_{-0.095}$	$-0.968^{+1.43}_{-1.63}$	$-69.43^{+1.62}_{-1.62}$	$0.412^{+0.026}_{-0.032}$	50.19 ± 0.24	1.130 ± 0.085	0.231 ± 0.004	$0.636^{+0.009}_{-0.010}$	$7.182^{+0.278}_{-0.281}$	—

^c km s⁻¹ Mpc⁻¹.^d H_IIG + QSO-AS + GRB.^e H_IIG + QSO-AS + GRB + QSO-Flux.^f $H(z)$ + BAO + H_IIG + QSO-AS + GRB.^g $H(z)$ + BAO + H_IIG + QSO-AS + GRB + QSO-Flux.^h This is the 1 σ limit. The 2 σ limit is set by the prior, and is not shown here.

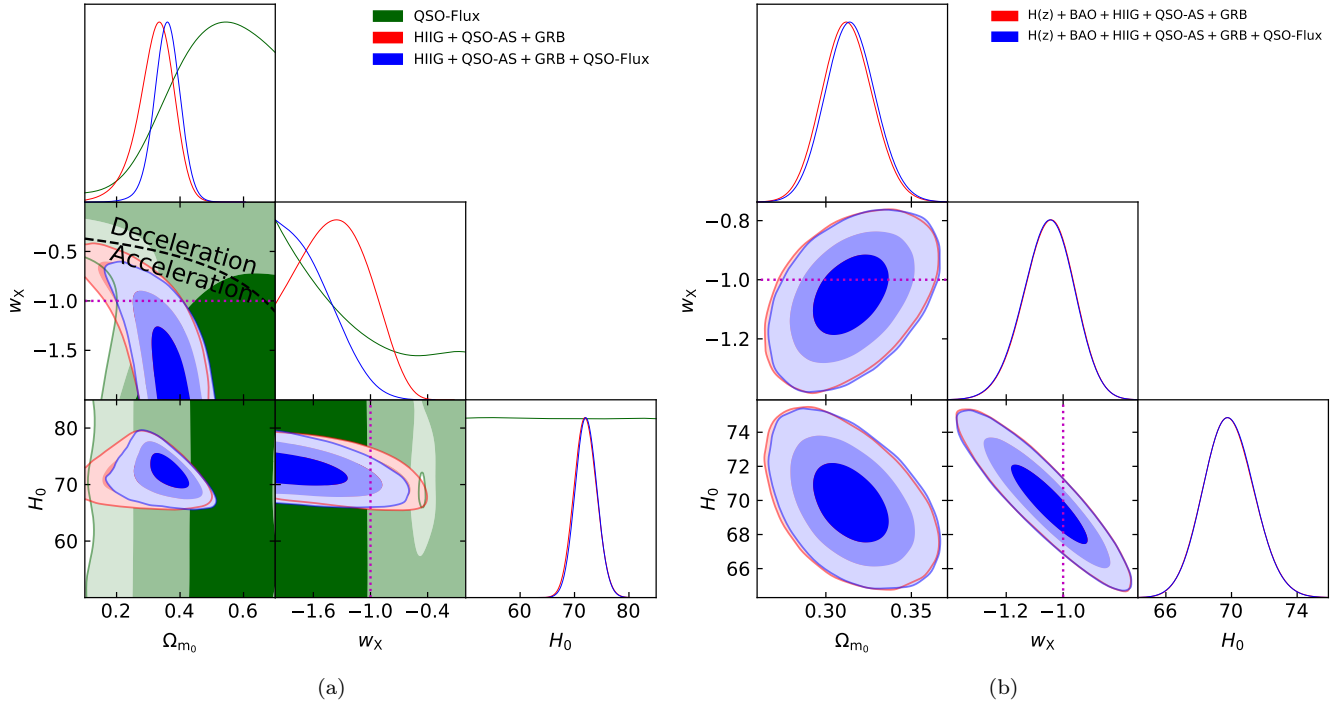


Figure A3. Same as Fig. 3 (flat XCDM) but for different combinations of data and showing only cosmological parameters.

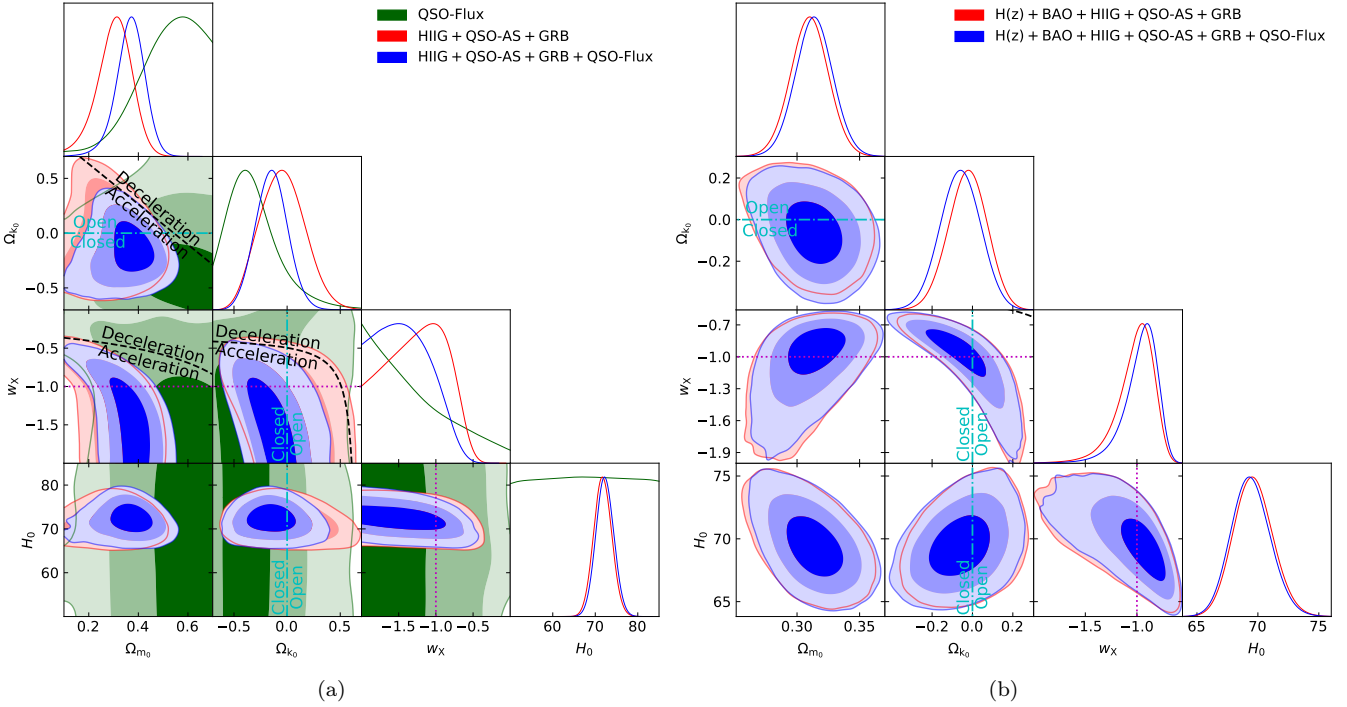


Figure A4. Same as Fig. 4 (non-flat XCDM) but for different combinations of data and showing only cosmological parameters.